Simulation of Particulate Matter Structure Detachment from Surfaces of Wall-Flow Filters for Elevated Velocities Applying Lattice Boltzmann Methods

Nicolas Hafen [1,2,3,*] **, Jan E. Marquardt** [2,3] **, Achim Dittler** [1,3] **and Mathias J. Krause** [2,3,4]

1   Gas Particle Systems, Karlsruhe Institute of Technology, 76131 Karlsruhe, Germany
2   Lattice Boltzmann Research Group, Karlsruhe Institute of Technology, 76131 Karlsruhe, Germany
3   Institute of Mechanical Process Engineering and Mechanics, Karlsruhe Institute of Technology, 76131 Karlsruhe, Germany
4   Institute for Applied and Numerical Mathematics, Karlsruhe Institute of Technology, 76131 Karlsruhe, Germany
*   Correspondence: nicolas.hafen@kit.edu; Tel.: +49-721-46575

Abstract: Rearrangement events in wall-flow filters lead to the formation of specific deposition patterns, which affect a filter's pressure drop, its loading capacity and the separation efficiency. A universal and consistent formulation of probable causes and influence factors does not exist and appropriate calculation models that enable a quantification of respective influence factors are missing. In this work, a previously developed lattice Boltzmann method, which has been used with inflow velocities of up to $2\,\mathrm{m\,s^{-1}}$, is applied to elevated velocities of up to $60\,\mathrm{m\,s^{-1}}$. The particle-free flow, a single layer fragment and a deposition layer during break-up are investigated as three different scenarios. One goal of this work is a comprehensive quantification of the stability and accuracy of both particle-free and particle-including flows, considering static, impermeable deposition-layer fragments. A second goal is the determination of the hydrodynamic surface forces and the deduction of the local detachment likelihood of individual layer fragments. Satisfactory stability and accuracy can be shown for fluid velocity, fluid pressure and the hydrodynamic forces. When considering layer fragments, the parameter domain turns out to be limited to inflow velocities of $28\,\mathrm{m\,s^{-1}}$. It is shown that fragment detachment rather occurs consecutively and regions of no possible detachment are identified. The work contributes to an understanding of rearrangement events and respective deposition pattern predictions and enables potential optimizations in engine performance, fuel consumption and the service life of wall-flow filters.

Keywords: wall-flow filter; lattice Boltzmann methods; porous media; resolved particle simulations; homogenized lattice Boltzmann method

1. Introduction

Wall-flow filters are one of the key components in modern exhaust treatment systems of internal combustion engines, enabling compliance with present emission limits [1]. By means of oppositely arranged inlet and outlet channels, such filters guide the introduced exhaust flow through porous walls, which separate the contained particulate matter (PM), with efficiencies up to 99% [2]. Over time, PM loading increases in the inflow channels, in which continuous deposition layers are formed on the porous wall surfaces, leading to an increase in pressure drop and resulting degradation in engine performance [3–5]. As the introduced PM mostly consists of combustible soot and small amounts of inorganic non-combustible ash, a filter's regeneration is achieved by continuously or periodically oxidizing its reactive components. Over long-term operation, this leads to an accumulation of ash, which forms agglomerates and affects the deposition layer composition. During regeneration, the resulting inhomogeneities can then lead to a break-up of the continuous layer into individual fragments, which can potentially detach from the filter surface

and relocate inside a channel's domain [3]. As a result, specific deposition patterns are formed, which affect a channel's pressure drop contribution, its loading capacity and the separation efficiency.

Probable causes and influence factors leading to the individual patterns have been determined in various scientific works [4,6–8]; however, a universal and consistent formulation without partially contradicting statements does not yet exist. Appropriate calculation models that enable a quantification of relevant influence factors are missing completely. This, however, impedes respective predictions on the formation of specific deposition patterns, which eventually affect engine performance, fuel consumption and the service life of wall-flow filters.

In Hafen et al. [9], the authors of the present manuscript demonstrated the applicability of surface-resolved particle simulations on the investigation of particulate matter structure detachment using lattice Boltzmann methods (LBM). Here, they presented a holistic LBM approach, which can be employed both for the simulation of the movement of resolved particles and the flow through porous media, while being based on the same numerical method. In the particle-free case, the presented model could be shown to exhibit super-linear grid convergence for an inflow velocity of $\bar{u}_{in} = 2.0 \, \mathrm{m \, s^{-1}}$ and good agreement with a reference solution, which had previously been validated thoroughly by experimental data [10]. Additionally, the approach could also be shown to enable the simulation of a transient detachment and transport process of surface-resolved structures governed by hydrodynamic forces. This work also includes a literature review addressing relevant findings on the deposition pattern formation, general numeric approaches to wall-flow filter modelling and LBM-related research regarding flow through porous media, as well as surface-resolved particle simulations.

In Hafen et al. [11], a holistic LBM approach was then used to investigate the detachment, acceleration and deceleration of individual particulate structures in order to derive clear predictions on the formation of specific deposition patterns. A pressure drop comparison with experimental investigations conducted on the experiment rig described in Thieringer et al. [12] led to the determination of a physically sensible substrate permeability of $K = 4.3 \times 10^{-12} \, \mathrm{m^2}$, which is adopted in the present work as well. General transport characteristics were determined, identifying several key parameters utilizable for a standardized comparison of different simulation and experiment runs. Eventually, the particle structure's pneumatic transport through the channel was investigated for different starting positions, substrate permeabilities, particle densities and inflow velocities up to $\bar{u}_{in} = 2.0 \, \mathrm{m \, s^{-1}}$.

In both works, the hydrodynamic forces acting on individual particulate structures were shown to be responsible for their detachment likelihood and transport characteristics under different operating and geometric conditions. While the described works, therefore, serve as a demonstration of the applicability of the simulation approach, the considered inflow velocities up to $\bar{u}_{in} = 2.0 \, \mathrm{m \, s^{-1}}$ only cover a small portion of the real world ranges that include velocities up to $\bar{u}_{in} = 80 \, \mathrm{m \, s^{-1}}$ [6]. The main focus of the present work is, therefore, to apply the developed LBM approach to an extended velocity range that covers as much as possible of the physically relevant domain. For a given discretization, however, elevated physical fluid velocities lead to the occurrence of higher LBM-specific lattice velocities, which inevitably drive a simulation closer to the method's inherent stability limit [13]. A discretization refinement increases the distance to the stability limit; however, this comes with the price of drastically increasing the amount of computational cells to be considered for three-dimensional simulations [11]. This, in turn, faces a limit due to the available computational resources, leading to the necessity of running a simulation with elevated fluid velocities in the vicinity of the stability limit. This has two implications: Firstly, the results' accuracy degrades [13] for both the individual quantities of interest and overall mass conservation. Additionally, the anisotropy of the flow (e.g., main flow direction vs. wall-penetration direction) leads to different magnitudes of differently oriented hydrodynamic force and torque contributions and respective different implications for their

accuracy. Secondly, local velocity peaks are more likely to break the stability locally, usually causing the simulation to diverge. The occurrence of the peaks is directly dependent on both the geometry of a wall-flow channel and specific deposition patters. As a consequence, a generic LBM discussion does not suffice and a wall-flow specific stability and accuracy examination is indispensable for the consideration of the elevated velocity range in the simulation approach.

One goal of the present work is, therefore, to provide a comprehensive quantification of the stability and accuracy of both particle-free and particle-including flow, considering static, impermeable PM layer fragments attached to the porous substrate's surface. For any future study intended to investigate three-dimensional flow in wall-flow filters with elevated velocities by means of the LBM, this work can serve as a foundation, providing insight into numerical borderline cases that need to be considered. A second goal is the determination of the hydrodynamic forces acting on the particulate structures and the deduction of the local detachment likelihood of individual layer fragments, including their dependency on local flow conditions and the layer's fragmentation. As the formation of specific deposition patterns is dominated by rearrangement events that require the occurrence of the detachment of such fragments, the present work represents a contribution to respective deposition pattern predictions.

The following sections provide an introduction to the mathematical modelling and relevant numerical methods (c.f. Section 2), a description of examined simulation cases for three specific scenarios (c.f. Section 3), and a discussion and interpretation of the study results (c.f. Section 4). A conclusion in Section 5 provides a summary of all the relevant findings and the resulting implications for wall-flow filter applications.

2. Mathematical Modelling and Numerical Methods

The present section briefly lays out the theoretical foundation for the simulation approach used in this work. This includes a description of the LBM principles in Section 2.1, an explanation of porous media and surface-resolved particle modelling (c.f. Section 2.3 and Section 2.2), and the quantification of errors and convergence behaviour (c.f. Section 2.4). A more detailed description on most aspects can, however, be found in Hafen et al. [9].

In this work, the evolution of conserved fluid quantities is described with the incompressible Navier–Stokes equations (NSE) [14]. With these, a fluid's velocity $u(x, t)$ and the pressure $p(x, t)$ at a three-dimensional position x in time t can be retrieved inside a specified domain. The fluid flow inside the porous substrate walls is modelled according to Darcy's law [15].

2.1. Lattice Boltzmann Method

One way of discretizing the continuous Navier–Stokes equation (NSE) is provided by the LBM in the form of a mesoscopic description of gas dynamics. Instead of individual molecules at the microscale, it considers a particle distribution function f and can be shown to lead to solutions of the equations of fluid dynamics on a macroscopic scale [13]. In this way, the LBM can be used as an alternative to conventional fluid methods, such as the finite volume method (FVM).

The discretization of the fluid domain is achieved by using a uniformly spaced voxel mesh with spacing δx. At time t and position x of the resulting lattice, the velocity space is discretized with lattice velocities c_i, leading to a set of corresponding discrete-velocity distribution functions f_i. While the size of these sets can be chosen in various ways, in the present work, $q = 19$ discrete velocities covering three spacial dimensions are considered. The lattice Boltzmann equation (LBE) describes the discrete-velocity distribution function f_i after a discrete time step δt at a neighbouring node, where a collision operator Ω_i accounts for the mesoscopic contribution of molecular collisions on the microscale. All lattice-related quantities can then be described in dimensionless lattice units by providing

some characteristic quantities inherent to the physics under study [13]. This allows for the commonly adopted choice of $\delta x = \delta t = 1$, leading to the LBE in the form

$$f_i(\boldsymbol{x} + \boldsymbol{c}_i, t+1) = f_i(\boldsymbol{x}, t) + \Omega_i(\boldsymbol{x}, t). \tag{1}$$

While the collisions can be modelled in various ways [16–18], in the present work, we adopt the choice of the previous works [9,11,19] and use a Bhatnagar–Gross–Krook (BGK) collision operator [16] with a lattice relaxation time of $\tau = 0.51$

$$\Omega_i(\boldsymbol{x}, t) = -\frac{1}{\tau}\left(f_i(\boldsymbol{x}, t) - f_i^{(eq)}(\boldsymbol{x}, t)\right). \tag{2}$$

It describes the relaxation of the discrete distribution function f_i towards its equilibrium $f_i^{(eq)}$ at a single fluid node

$$f_i^{(eq)}(\boldsymbol{u}, \rho) = w_i \rho \left[1 + \left(\frac{\boldsymbol{c}_i \cdot \boldsymbol{u}}{c_s^2} + \frac{(\boldsymbol{c}_i \cdot \boldsymbol{u})^2}{2c_s^4} + \frac{\boldsymbol{u}^2}{2c_s^2}\right)\right] \tag{3}$$

with weights w_i and a lattice speed of sound of $c_s = 1/\sqrt{3}$ inherent to the velocity set chosen in this work [13]. With (2) and (3), a link to local macroscopic fluid quantities can be established: According to the Chapman–Enskog analysis [20], the macroscopic kinematic viscosity can be shown to depend on the relaxation time as

$$\nu = c_s^2 \left(\tau - \frac{1}{2}\right). \tag{4}$$

The equilibrium function $f_i^{(eq)}$ in (3), in turn, depends on the macroscopic fluid density ρ and the macroscopic fluid velocity $\boldsymbol{u}$, which can be retrieved via the zeroth- and first-order moments of the discrete distribution function

$$\rho = \sum_{i=0}^{q-1} f_i \quad \text{and} \quad \rho\boldsymbol{u} = \sum_{i=0}^{q-1} \boldsymbol{c}_i f_i. \tag{5}$$

With the lattice speed of sound c_s, the density ρ can be related to the pressure p at lattice scale via the isothermal equation of state

$$p = c_s^2 \rho. \tag{6}$$

One of the key features of the LBM is the possibility of splitting (1) into a purely local collision and a subsequent streaming step. This enables an efficient parallelization strategy, which is realized in the open source software OpenLB [21], used in the present work.

2.2. Porous Media Modelling

Within the LBM, the momentum loss that a fluid experiences when passing through a porous medium according to Darcy's law can be accounted for by means of an effective velocity [22]. The relaxation time τ, the kinematic fluid viscosity ν and the medium's permeability K can be expressed in the form of a *confined permeability* $d \in [0, 1]$ [9] as they stay constant throughout a simulation. This leads to

$$\boldsymbol{u}^{eff}(\boldsymbol{x}, t) = d\boldsymbol{u}(\boldsymbol{x}, t) \quad \text{with} \quad d = 1 - \tau\frac{\nu}{K}. \tag{7}$$

2.3. Surface-Resolved Particle Simulations

The homogenized lattice Boltzmann method (HLBM) [23–25] represents a generalization of (7) to surface-resolved particles by considering moving porous media. By associating a local confined permeability $d(\boldsymbol{x}, t)$ with a local weighting factor $B(\boldsymbol{x}, t) \in [0, 1]$ as a *cell*

saturation, differentiating between sole liquid ($B = 1$), sole solid ($B = 0$) and mixed ($0 < B < 1$) contributions at every node with position $\boldsymbol{x}$, the approach represents a specific form of the partially saturated method (PSM) [26–28]. In order to avoid fluctuations, a smooth transition layer of width ϵ is used symmetrically at the boundary of a single particle with index k. The weighting factor in this layer can, thus, be described with the particle's centre of mass $X_k(t)$ and a given point $\vec{x}$ on an outward-facing normal of the surface via

$$B(\vec{x}, t) = \cos^2\left(\frac{\pi}{2\epsilon}(\|X_k(t) - \vec{x}\|_2)\right). \tag{8}$$

The factor is then used to determine a weighted average of the fluid velocity $\boldsymbol{u}$ and the solid particle velocity $\boldsymbol{u}^S$ at a single node

$$\boldsymbol{u}^{eff}(\boldsymbol{x}, t) = B(\boldsymbol{x}, t)\boldsymbol{u}(\boldsymbol{x}, t) + (1 - B(\boldsymbol{x}, t))\boldsymbol{u}^S(\boldsymbol{x}, t), \tag{9}$$

which then enters the LBE. While the approach enables the simulation of dynamic particle movement [9,11,19,23–25,29], the consideration of immobile particles ($\boldsymbol{u}^S = 0$) in the present work simply reduces (9) to (7). More details on the particle's shape representation providing the respective normal and the HLBM's derivation can be found in Trunk et al. [24,25].

While the described methodology enables the modelling of the particle's influence on the fluid field, the back coupling is achieved by employing a momentum exchange approach at a particle's surface. Analogously to the previous works [9,11,19], the one originally proposed by Wen et al. [30], but extended for smooth interfaces by Trunk et al. [24], is used in the present work. The force contribution of every node $\boldsymbol{x}_b$ in the smooth boundary transition area of a single particle k can be retrieved via

$$\boldsymbol{F}_k(\boldsymbol{x}_b, t) = \sum_{i=0}^{q-1}\left[(\boldsymbol{c}_i - \boldsymbol{u}^S(t))f_i(\hat{\boldsymbol{x}}_b, t+1) - (\boldsymbol{c}_{\bar{i}} - \boldsymbol{u}^S(t))f_{\bar{i}}(\boldsymbol{x}_b, t+1)\right] \tag{10}$$

by calculating the differences between the discrete velocities $\boldsymbol{c}_i$ and the particle's solid velocity $\boldsymbol{u}^S$. The next node in the direction of i is denoted $\hat{\boldsymbol{x}}_b$. Index $\bar{i}$ denotes the opposite direction of it. With it, the force $\boldsymbol{F}_k$ and torque $\boldsymbol{T}_k$ acting on a particle's centre of mass $\boldsymbol{X}_k$ can then be retrieved by summing the individual force contributions over all boundary nodes $\boldsymbol{x}_b$ via

$$\boldsymbol{F}_k(t) = \sum_{\boldsymbol{x}_b}\boldsymbol{F}_k(\boldsymbol{x}_b, t) \quad \text{and} \quad \boldsymbol{T}_k(t) = \sum_{\boldsymbol{x}_b}(\boldsymbol{x}_b - \boldsymbol{X}_k(t))\boldsymbol{F}_k(\boldsymbol{x}_b, t). \tag{11}$$

2.4. Quantification of Errors and Convergence

In order to assess a simulation's transient convergence behaviour, a respective criterion is defined as the standard deviation σ of a quantity χ being smaller than a predefined residuum r multiplied by the average $\bar{\chi}$ over the last T time steps

$$\sigma(\chi) = \sqrt{\frac{1}{T+1}\sum_{t=1}^{T}(\chi_t - \bar{\chi})^2} < r\bar{\chi}. \tag{12}$$

For the convergence evaluation of a particle's surface force, $\boldsymbol{F}_k$ or $\boldsymbol{T}_k$ from (11) can be used directly as quantity χ. Convergence of the fluid's velocity and pressure, are, however, evaluated via the kinetic energy and the lattice density averaged by the total cell number M

$$\chi_t(\boldsymbol{u}) = \frac{1}{M}\sum_{m=1}^{M}\left(\frac{1}{2}\|\boldsymbol{u}\|^2\right)_m \quad \text{and} \quad \chi_t(\rho) = \frac{1}{M}\sum_{m=1}^{M}\rho_m \tag{13}$$

right after being calculated via the moments according to (5).

The influence of a discretization refinement is assessed by evaluating the grid convergence, where the error err_{L^2} based on the L^2 norm is used as an error criterion for a quantity χ at a given resolution N

$$err_{L^2}(\chi) = \sqrt{\frac{\sum_{m=1}^{M}\left(\chi_m^{\mathrm{ref}} - \chi_m\right)^2}{\sum_{m=1}^{M}\left(\chi_m^{\mathrm{ref}}\right)^2}}. \tag{14}$$

3. Application to a Wall-Flow Filter

In this work, the simulation setup of a single wall-flow channel, as described in the previous works [9,11,19], is adopted and shown in Figure 1.
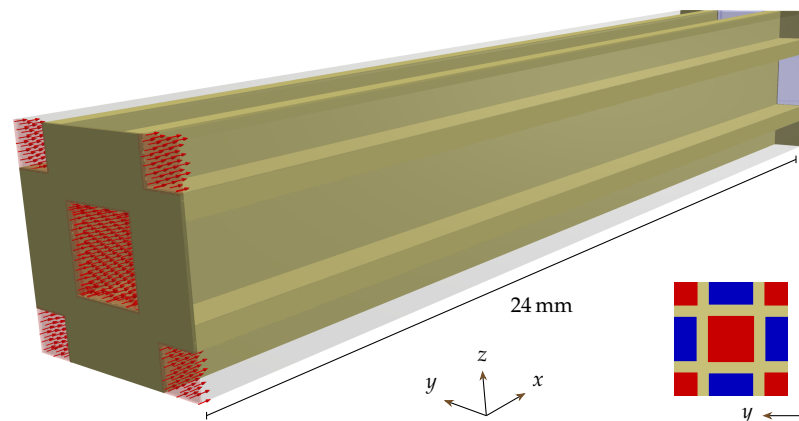
Figure 1. Channel model, including one central inflow channel and fractions of surrounding inflow and outflow channels. Dark yellow structures represent porous filter substrate, brown structures solid walls. Red colouring indicates inflow sections, blue colouring indicates outflow sections.

It consists of a porous structure with a substrate permeability of $K = 4.3 \times 10^{-12}\,\mathrm{m^2}$ and a wall thickness of $l_w = 0.4\,\mathrm{mm}$, which separates a central inflow channel, four additional quarter-sized inlet channels and four half-sized outflow channels. The channels have a width of $l_y = 1.6\,\mathrm{mm}$, which serves as the reference length for the spatial resolution N, defined as the number of cells per channel width. A scaled channel length of $l_{x,s} = 24\,\mathrm{mm}$ is used, which accounts for a fifth of a real world representative of $l_x = 120\,\mathrm{mm}$. This scaling leads to the great reduction in computational demand that enables the extensive studies in the present work in the first place, while ensuring similar flow characteristics, which is shown in Hafen et al. [11]. It should be noted, however, that, for a given flux, a length reduction leads to a higher wall throughput, which results in an increased overall pressure drop, impeding a direct comparison with experimental results. The temperature in a wall-flow filter can vary significantly both on average and locally depending on the operating conditions [1]. As temperature effects, however, are not part of the present work's scope, ambient conditions are assumed for the whole channel domain.

The model's symmetry enables the application of periodic boundary conditions on the four surrounding sides, which let it serve as a representation of a real wall-flow filter comprised of hundreds of individual channels. A constant velocity at the inlets and a constant pressure at the outlets is imposed using Dirichlet boundary conditions [14]. Solid walls at the channel end caps on both sides are modelled with a no-slip condition. The LBM realization of the latter is performed with a simple bounce-back condition [31], and regularized local boundary conditions [32] are used at the outlet. As the studies in the previous works suffered from severe stability issues for inflow velocities above $\bar{u}_{in} = 2.0\,\mathrm{m\,s^{-1}}$, the local boundary condition at the inflow is exchanged for an interpolated one [33], which has been found to generally yield more stable results.

Three different scenarios are investigated with dedicated purposes for each in the present work:

1. Particle-free flow
2. Single layer fragment
3. Deposition layer during break-up

First, the *particle-free flow* in a clean channel is investigated in order to define and examine the parameter domain that represents a necessary stability criterion for the wall-flow model under study. In the second scenario, a *single layer fragment*, attached to the porous wall's substrate, is considered. For this, the parameter domain is re-evaluated, this time including the individual components of the hydrodynamic force acting on the fragment's surface. The third scenario represents a *deposition layer during break-up*. With it, local effects on the fluid field and the acting forces are investigated for different situations along the channel. The spatial distribution of hydrodynamic forces is evaluated in order to derive predictions on the detachment likelihood of individual layer fragments and their mutual influence. Independent of the scenario, all simulations are run until either reaching the convergence criteria for the characteristic quantities of interest, diverging or exceeding a defined maximum simulation time when fluctuations emerge. The respective residuals for the average kinetic energy and the average lattice density of $r_u = 10^{-7}$ and $r_\rho = 10^{-6}$ are adopted from the previous works [9,11,19]. For particle-related scenarios, the convergence is defined as reaching convergence for both fluid quantities and the normal component of the hydrodynamic force additionally, for which the residuum is set to $r_F = 10^{-7}$.

3.1. Particle-Free Flow

In order to investigate the stability and accuracy of the particle-free flow, the wall-flow model including the specified set of boundary conditions and LBM collision dynamics is used for simulations, considering filtration relevant inflow velocities of $\bar{u}_{in} = 2 \text{ m s}^{-1}$ to 60 m s^{-1}. Spatial resolutions between $N = 32$ and 128 are considered, which are defined as the number of cells per channel width l_y. In an attempt to derive clear predictions for an inflow velocity threshold, the macroscopic quantity $\bar{u}_{in}$ is related to its LBM specific lattice counterpart $\bar{u}_{in,L}$ via

$$\bar{u}_{in} = \bar{u}_{in,L} c_u. \tag{15}$$

The respective conversion factors for velocity, position and time

$$c_u = \frac{c_x}{c_t} \quad \text{with} \quad c_x = \frac{L_{char}}{N} \quad \text{and} \quad c_t = (\tau - 0.5)c_{s,L}^2 \frac{1}{\nu}\left(\frac{L_{char}}{N}\right)^2 \tag{16}$$

result from the non-dimensionalization approach, commonly employed for the relation between macroscopic and lattice quantities [13].

3.2. Single Deposition Layer Fragment

The investigation of a single deposited PM layer fragment allows for the isolated evaluation of the accuracy and velocity dependency of relevant surface forces. While such a fragment only has a minor effect on the global fluid field, it represents an obstacle in the flow that can lead to locally increased velocities. These may, in turn, cause divergence for smaller inflow velocities with respect to the particle-free case. A separate stability evaluation is therefore inevitable. Additionally, it should be considered that the channel's base resolution of $N = 16$ has been chosen in such a way that a constant ratio between channel width and the thickness of the porous walls can be ensured, while maintaining complete symmetry of the model for multiples of the base resolution [9]. Fragments of the deposition layer, however, are subject to stepwise occurring anisotropic discretization effects of the particle surface, potentially leading to fluctuations in the grid convergence of the force components. Therefore, resolutions up to $N = 176$ are considered to, nevertheless, provide a representative data basis.

Analogously to Hafen et al. [11], a single fragment is placed flush on the substrate's surface. The structure is represented by a cubical disk with an edge ratio of $2 \times 2 \times 1$ and a base size of $d_z = 170 \,\mu\text{m}$. At this point, it should be reiterated that, regarding the employed

momentum exchange approach, the substrate wall is not considered solid. It is rather part of the global fluid field with a decreased permeability according to (7). This ensures that all fluid nodes necessary to prevent failure of the momentum exchange approach are provided. The channel model with a single PM layer fragment is shown in Figure 2.
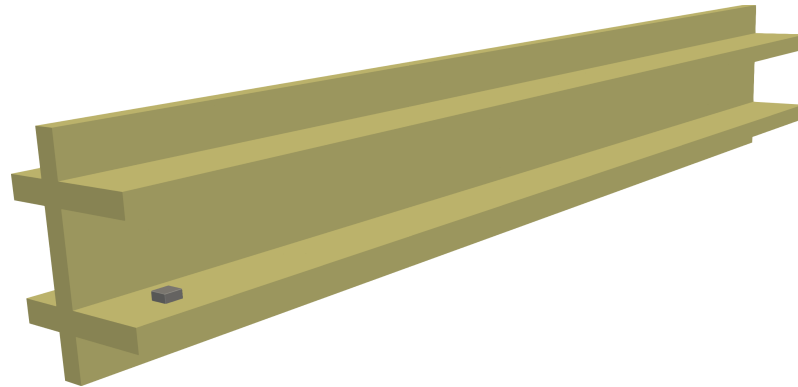
Figure 2. Channel model featuring a single PM layer fragment in gray. Dark yellow structures represent porous filter substrate.

In Hafen et al. [11], it could be deduced that the normal forces acting on a fragment's surface cannot contribute much to its detachment. Tangential forces were, in turn, shown to be larger by at least a factor of four in every considered case. This led to the conclusion that, for equally shaped fragments, a lift-off can only be achieved by a rotational movement over the fragment's back-side edge. In order to enhance the modelling of this process, a *rotation-induced normal force* $F_{N,rot}$ is additionally considered in the present work. All relevant forces are outlined in Figure 3.
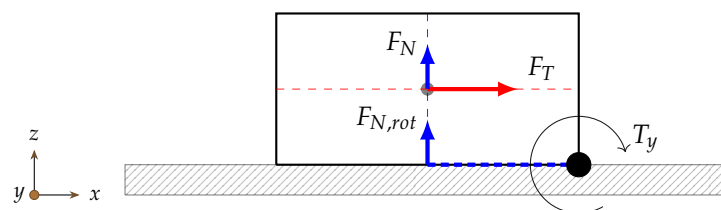
Figure 3. Sketch of single PM layer fragment and considered hydrodynamic forces. Tangential contributions red, normal contributions blue. Torque around y-axis at eccentric contact line.

The standard normal and tangential force F_N and F_T are retrieved as components of the force $\boldsymbol{F}_k$ that results from summing the individual contributions of the momentum exchange approach at all surface boundary nodes $\boldsymbol{x}_b$ according to (11). The calculation of the torque $\boldsymbol{T}_k$, however, additionally requires the specification of a centre of rotation, usually represented by a particle's centre of mass $\boldsymbol{X}_k$. Using the actual contact line assumed for a rotational detachment (c.f. Figure 3) as the centre of rotation instead, the torque T_y can be calculated directly at this position with the momentum exchange approach. Its contribution to a *normal directed detachment* can then be modelled via the *rotation-induced normal force* $F_{N,rot}$, which simply results from dividing the torque T_y by half of the fragment's x-dimension as the rotational lever.

3.3. Deposition Layer during Break-Up

As a final scenario, a deposition layer during break-up due to the oxidization of the majority of its soot content [3] is investigated. Analogously to Hafen et al. [9], the layer fragments are modelled as a field of identical cubic discs that cover the porous walls inside an inflow channel. For these, the same characteristics as described in the single particle scenario are assumed. As a base configuration, a uniform field of 3×40 fragments

is considered on each of the four porous walls. The channel model with a uniformly fragmented PM layer is shown in Figure 4.
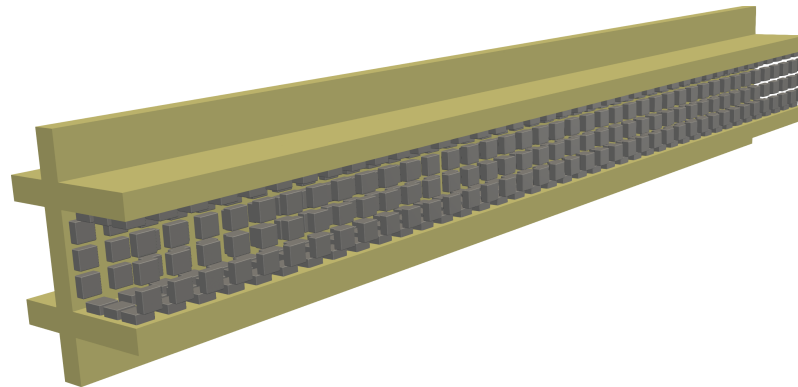
Figure 4. Channel model with uniformly fragmented PM layer in gray. Dark yellow structures represent porous filter substrate.

In order to additionally investigate the effect of the filter loading, non-uniform oxidization kinetics and the temporal evolution of the break-up process, four modifications are considered: By varying the layer height, the amount and predominant deposition location of introduced PM can be accounted for. In this context, the layer height is either varied uniformly or by assuming a predefined transition region, as laid out in Figure 5.

(**a**) uniform (**b**) increasing
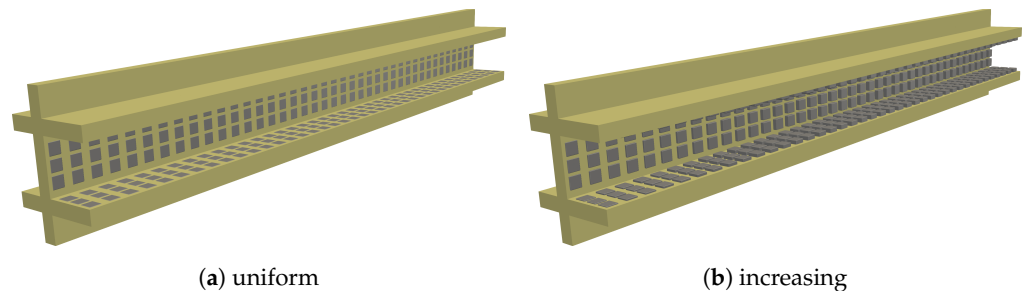
Figure 5. Channel model with modified PM layer height.

While a uniform variation of the layer height in Figure 5a is supposed to represent a simple approach to account for the duration of loading and the PM concentration, an initially increasing layer height in Figure 5b resembles layer characteristics reported in the literature [34,35]. For the latter, a PM layer with increasing height over a relative channel length of x_{rel} in the channel's front section is considered.

With a modification of the substrate coverage, the temporal evolution during regeneration can be modelled by accounting for local differences in the progress of soot oxidization or by regarding an advanced point in time when some detachment has already occurred. This is realized by considering non-uniform layer fragmentation and partial detachment, as shown in Figure 6.

(**a**) non-uniform layer fragmentation (**b**) partial detachment
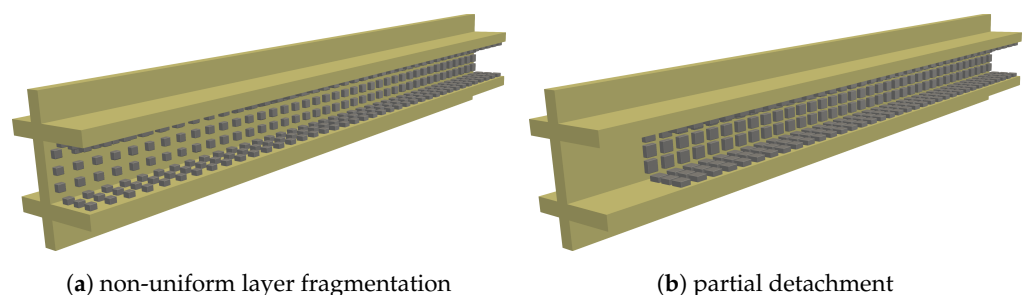
Figure 6. Channel model with modified substrate coverage.

The non-uniform layer fragmentation in Figure 6a features an increasing substrate coverage, beginning from a relative fragment size of $d_{xy,rel}$ to the one assumed in the base configuration. In order to evaluate the impact, each layer configuration is compared against its inverted counterpart, which, respectively, features a decreasing coverage, ending with the relative fragment size at the channel's back. For the partial detachment in Figure 6b, layer structures with multiple rows removed over a relative channel length x_{rel} are considered.

4. Results and Discussion

In the following, the simulation results will be presented and discussed for all three scenarios described in Sections 3.1–3.3. While resolutions up to $N = 176$ are considered, flow-field visualizations are generally extracted from $N = 96$ data sets due to much smaller memory consumption.

4.1. Particle-Free Flow

The particle-free flow is investigated regarding its transient convergence behaviour of the fluid pressure and velocity (c.f. Section 4.1.1), the resulting flow field (c.f. Section 4.1.2) and the grid convergence as a measure of accuracy (c.f. Section 4.1.3).

4.1.1. Transient Convergence Behaviour

In order to determine the necessary stability domain, simulations with different combinations of average inflow velocity $\bar{u}_{in}$ and resolution N are run until completion (c.f. Section 3). The actual value of each convergence quantity is then evaluated, considering three possible states: *convergence* is assumed if the value has passed its predefined residuum. Undefined values due to a division by zero are counted as *diverged*. A completion triggered by the specified maximum simulation time of $t_{max} = 0.1\,\text{s}$, is considered a *timeout*, which can be caused by both continuously fluctuating quantities or a very slow convergence behaviour, rendering the simulation unfeasible. The resulting stability map is shown in Figure 7. Generic LBM limits according to (15) assuming relevant lattice velocities are included as well. The resulting stability map is shown in Figure 7.
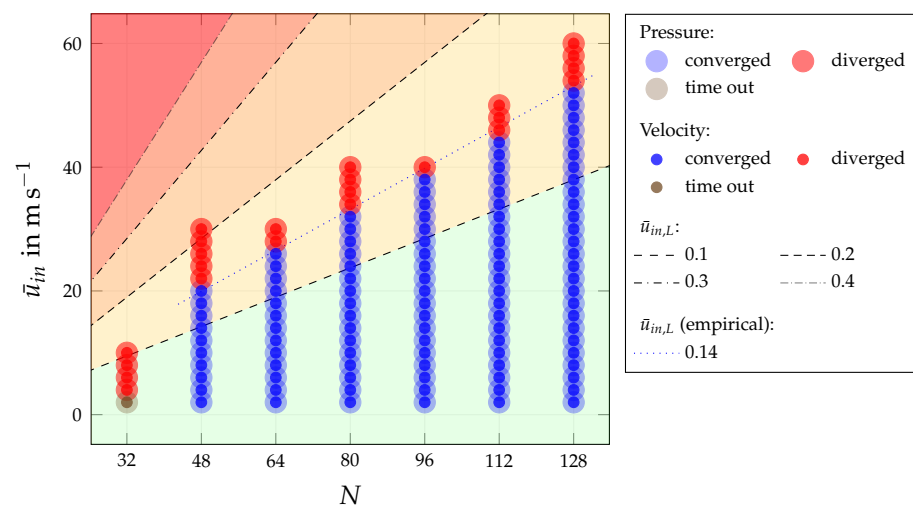
Figure 7. Stability map for pressure and velocity convergence in particle-free flow. Contour lines show stability-relevant and empirically determined velocities at lattice scale. Background colouring indicates distance to theoretical LBM stability limits (green to red).

The first thing to note is that pressure and velocity exhibit synchronous convergence behaviour. For a resolution of $N = 32$ cells per channel diameter, no convergence can be achieved within the considered duration. With a resolution of $N = 48$, inflow velocities up to $\bar{u}_{in} = 20\,\text{m s}^{-1}$ can be realized. Increasing resolutions, then, enable convergence for

higher inflow velocities as well, reaching up to $\bar{u}_{in} = 52\,\mathrm{m\,s^{-1}}$ at $N = 128$. It becomes apparent that the resulting stability threshold follows a linear course with a slope that fits well between those of the contour lines for $\bar{u}_{in,L} = 0.1$ and 0.2. The considered wall-flow model can, accordingly, generally be assumed to be capable of handling inflow velocities that lead to an average lattice velocity smaller than $\bar{u}_{in,L,max} \approx 0.14$. Taking (16) into account, this allows the formulation of a resolution-dependent maximum inflow velocity via

$$\bar{u}_{in,max}(N) = AN \qquad \text{with} \qquad A = \bar{u}_{in,L,max}\frac{c_u}{N} = 0.14\frac{\nu}{(\tau - 0.5)c_{s,L}^2 L_{char}} = 0.415 \quad (17)$$

4.1.2. Flow Field

The resulting flow field for an inflow velocity of $\bar{u}_{in} = 20.0\,\mathrm{m\,s^{-1}}$ and a resolution of $N = 96$ is shown in Figure 8.
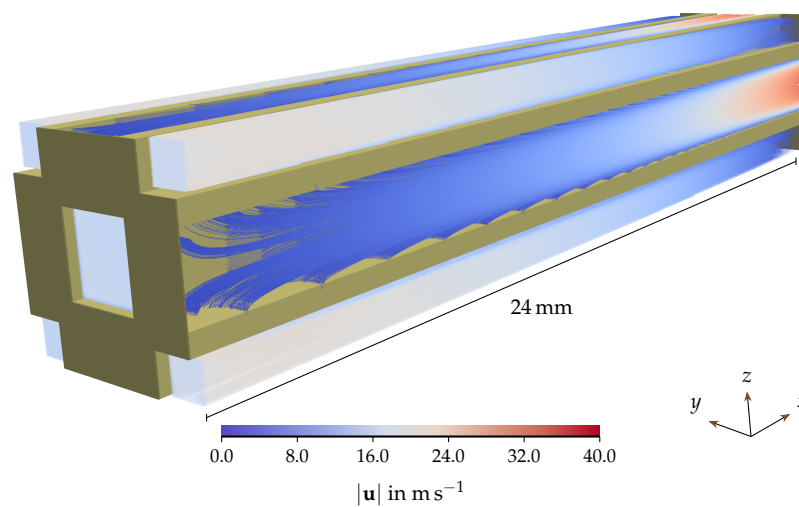
Figure 8. Particle-free flow with an inflow velocity of $\bar{u}_{in} = 20.0\,\mathrm{m\,s^{-1}}$ and a resolution of $N = 96$. Dark yellow structures represent porous filter substrate, brown structures solid walls. Streamlines exhibit local flow direction. Colour scale indicates local velocity magnitude.

The channel model from Figure 1 shows coloured streamlines according to the local flow direction and magnitude. Starting with the prescribed inflow velocity, the five inlet channels exhibit a decreasing velocity magnitude and streamline density along their length. The outflow channels, in turn, show a continuous magnitude and density increase, eventually forming a developed channel profile at the outflow. The parabolically shaped profile solely results from the momentum loss in the enclosing porous walls, as no specific modelling of friction is considered. The resulting presence of elevated velocities of up to $|\mathbf{u}| = 32.8\,\mathrm{m\,s^{-1}}$ drives the simulation closer to the stability limit, proving the necessity for a model-specific stability discussion.

The axial fluid velocity and the pressure averaged at discrete locations over the inflow and outflow channels' cross-sections $\bar{u}_x$ and $\bar{p}$, are shown in Figure 9 for different inflow velocities. In order to include inflow velocities up to $\bar{u}_{in} = 40.0\,\mathrm{m\,s^{-1}}$, a resolution of $N = 128$ is considered here. Due to their location inside the solid wall, the last position in the inflow channel ($x = 24\,\mathrm{mm}$) and the first one in the outflow channel ($x = 0\,\mathrm{mm}$) do not produce any fluid information.
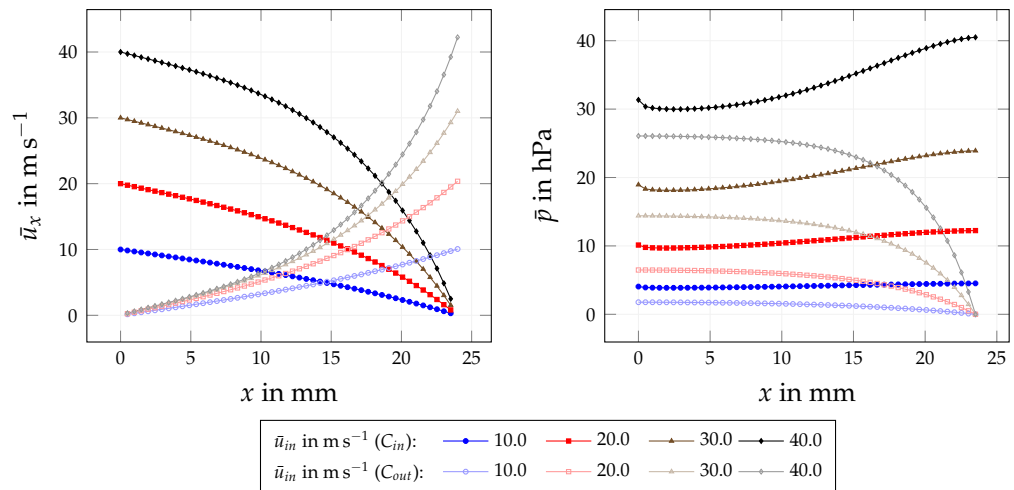
Figure 9. Velocity profiles $\bar{u}_x(x)$ and pressure profiles $\bar{p}(x)$ in inlet channel domain C_{in} and outlet channel domain C_{out} with a resolution of $N = 128$.

The velocity $\bar{u}_x$ in the inflow channel domain C_{in} transitions from the imposed one at the inlet $\bar{u}_{in}$ to zero at the channel end in the form of a distinctive curve for all inflow velocities considered. The fluid passing through the porous filter walls then accumulates in the outflow channel domain C_{out}, which exhibits the opposite behaviour accordingly. For velocities in the close vicinity of the stability limit, mass conservation degrades, leading to a difference between the resulting average axial fluid velocity at the outlets and the imposed one at the inlets. The pressure profile of the inlet channel also exhibits a distinctive form at a pressure level resulting from the momentum loss due to the porous walls between the channels. Near the inflow channel's back wall, the pressure reaches its maximum value. The average pressure in the outflow channel decreases continuously with a decreasing slope. In this way, the pressure difference between the inflow and outflow channel continuously increases over the channel length.

4.1.3. Grid Convergence

The final values of the average kinetic energy $\bar{E}_{kin}$ and average lattice density $\bar{\rho}$, as representatives of the velocity and pressure convergence, are then used to calculate the respective $err_{L^2}(\chi)$ according to (14), with the highest resolution of $N = 128$ as the reference solution χ^{ref}. The grid convergence for four different inflow velocities is shown in Figure 10.

Both quantities can be shown to exhibit a quadratic or super-quadratic experimental order of convergence (EOC) over the considered resolution range. The velocity convergence, however, features a relatively large error level, which is nearly identical for all inflow velocities. The pressure convergence, in turn, exhibits a smaller error level, which increases significantly for greater inflow velocities. Based on this, it can be assumed that the wall-flow model including the porosity approach is consistent with respect to the chosen grid resolution and is generally able to recover the flow for velocities up to $\bar{u}_{in} = 40\,\text{m}\,\text{s}^{-1}$. Due to the in-part high error level, however, the highest resolution feasible should always be used. From the average density's error, it can additionally be deduced that mass conservation might depend slightly on the inflow velocity.
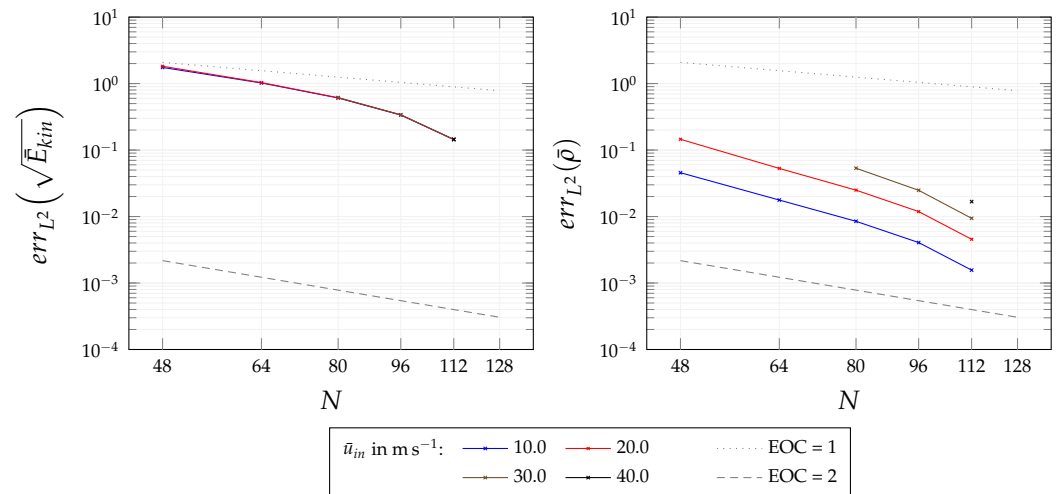
Figure 10. Error err_{L^2} of final values of average kinetic energy and average lattice density for different inflow velocities $\bar{u}_{in}$. Reference solution χ^{ref} at $N = 128$. Quadratic and linear EOC as guidelines.

4.2. Single Deposition Layer Fragment

Analogously to the particle-free flow, the transient convergence behaviour (c.f. Section 4.2.1), the resulting flow field (c.f. Section 4.2.2) and the grid convergence (c.f. Section 4.2.3) are investigated for a single layer fragment attached to the porous wall's substrate.

4.2.1. Transient Convergence Behaviour

The final state of the transient convergence behaviour is evaluated for different inflow velocities $\bar{u}_{in}$ and resolutions up to $N = 176$. As laid out in Section 3, the normal component of the force acting on a fragment's surface is used additionally as a third convergence quantity. The resulting stability map is shown in Figure 11.
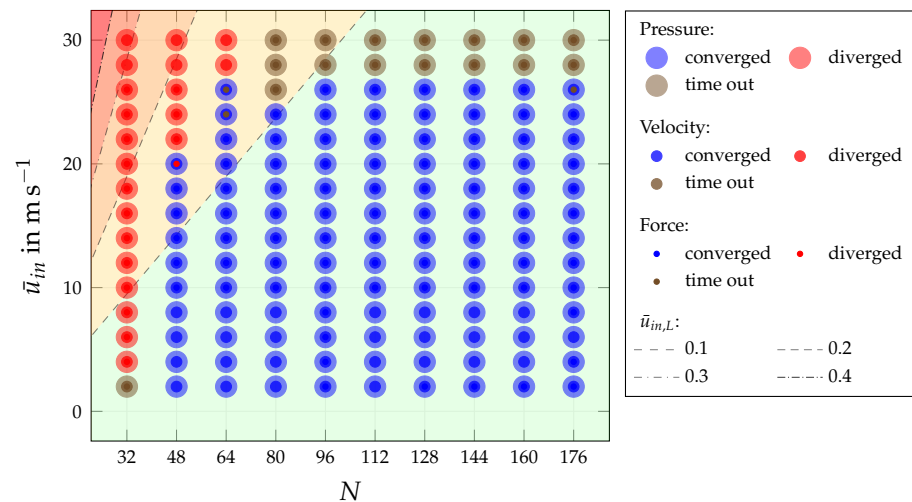
Figure 11. Stability map for pressure, velocity and force convergence in flow with single layer fragment. Contour lines show stability-relevant velocities at lattice scale. Background colouring indicates distance to theoretic LBM stability limit (green to red).

For resolutions up to $N = 64$, the same convergence threshold can be observed for the flow as in the particle-free scenario. Larger resolutions, however, do not enable the flow convergence for inflow velocities greater than $\bar{u}_{in} = 26\,\mathrm{m\,s^{-1}}$ due to persisting fluctuations in the fluid field. These can be reasoned rather to represent a physically correct

behaviour than numerical artefacts as an increase in the grid resolution does not change their occurrence. The force convergence mostly shares the same behaviour as the pressure and velocity, but, for some specific cases, exhibits time out and divergence states for slightly smaller inflow velocities. As a result, the following particle-related studies are limited to inflow velocities smaller than $\bar{u}_{in} = 28\,\mathrm{m\,s^{-1}}$.

In order to confirm these observations, the transient behaviour of the velocity criterion is shown in Figure 12 for a resolution of $N = 96$ and different inflow velocities.
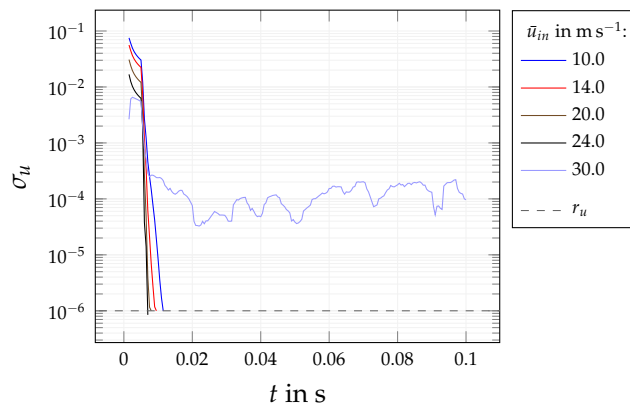
Figure 12. Transient development of velocity convergence with a resolution of $N = 96$ for different inflow velocities $\bar{u}_{in}$. Dashed line represents residuum $r_{\bar{u}}$.

For inflow velocities up to $\bar{u}_{in} = 26\,\mathrm{m\,s^{-1}}$, convergence can be achieved within less than $t = 0.02\,\mathrm{s}$, while smaller velocities generally lead to a slower convergence. An inflow velocity of $\bar{u}_{in} = 30\,\mathrm{m\,s^{-1}}$, in contrast, results in a continuously fluctuating behaviour around $\sigma_u = 1 \times 10^{-4}$, rendering it impossible to obtain a converged fluid field with respect to the specified residuum of $r_u = 1 \times 10^{-6}$. In order to ensure convergence with a sufficient distance to the convergence limit, an inflow velocity of $\bar{u}_{in} = 20\,\mathrm{m\,s^{-1}}$ is used for all following particle-related studies. The respective transient behaviour of all three convergence quantities for a resolution of $N = 96$ is shown in Figure 13.
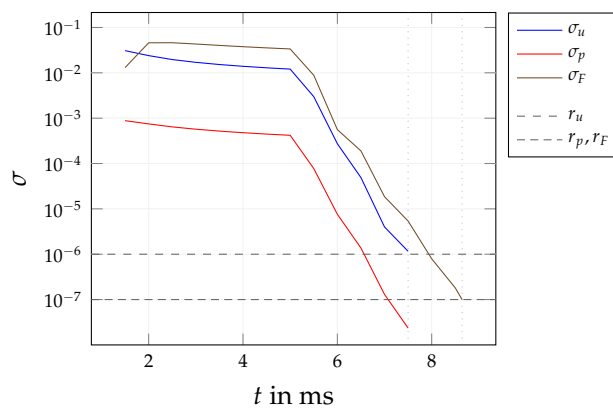
Figure 13. Transient development of velocity, pressure and force convergence for an inflow velocity of $\bar{u}_{in} = 20\,\mathrm{m\,s^{-1}}$ with a resolution of $N = 96$. Dashed lines represent residuals r_u, r_p and r_F. Dotted lines indicate time of flow and force convergence.

All convergence quantities show a similar behaviour: After a short transition period, the quantities head towards their respective residuum with a similar slope. The fluid field converges first at $t = 7.5\,\mathrm{ms}$, but is followed shortly by the convergence of the hydrodynamic force on the particle surface at $t = 8.65\,\mathrm{ms}$. This shows that all quantities are strongly coupled, but suggests that fluid convergence generally has to be ensured first.

4.2.2. Flow Field

The flow field around the single fragment is shown in Figure 14 for an inflow velocity of $\bar{u}_{in} = 20.0\,\mathrm{m\,s^{-1}}$ and a resolution of $N = 96$.
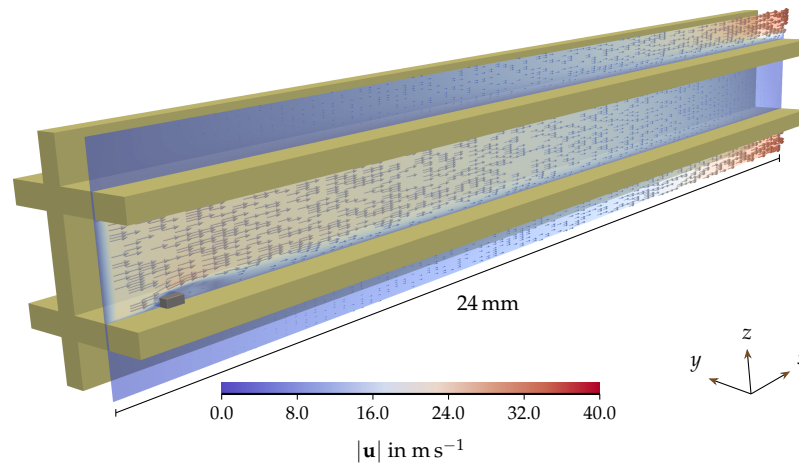
Figure 14. Flow field with an inflow velocity of $\bar{u}_{in} = 20.0\,\mathrm{m\,s^{-1}}$ and a resolution of $N = 96$ featuring a single PM layer fragment in gray. Dark yellow structures represent porous filter substrate. Colour scale indicates local velocity magnitude.

Due to its small dimensions, the fragment does not lead to great differences in the global fluid field with respect to the one in the particle-free case. In the direct vicinity of the fragment, however, an acceleration of the local fluid velocity can be observed on the fragment's upper side. In the shielded area right behind it, a region of greatly reduced velocity can be found, which is large enough to potentially influence the flow conditions at neighbouring fragments.

The influence of the inflow velocity on all three force variants is shown in Figure 15.
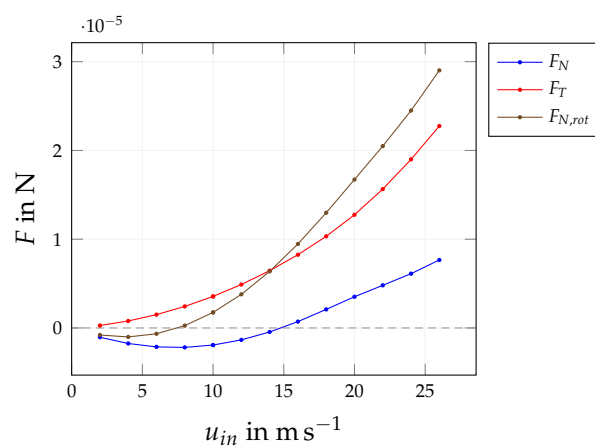
Figure 15. Comparison of standard normal force F_N, tangential force F_T and rotation-induced normal force $F_{N,rot}$ at convergence with a resolution of $N = 96$ for different inflow velocities.

All forces feature small values for velocities close to zero, but increase continuously for higher velocities. While the tangential force F_T is always positive, the standard normal and rotation-induced normal forces F_N and $F_{N,rot}$ only exhibit positive values for inflow velocities greater than $\bar{u}_{in} = 15\,\mathrm{m\,s^{-1}}$ and $\bar{u}_{in} = 8\,\mathrm{m\,s^{-1}}$, respectively. In accordance with the observations in Hafen et al. [11], this shows that detachment of particle structures with similar form can most likely only be caused by tangential forces when considering smaller inflow velocities. The rotation-induced normal force is always greater than the standard normal force and even becomes greater than the tangential one after $\bar{u}_{in} = 15\,\mathrm{m\,s^{-1}}$. Normal

induced detachment assuming a non-slipping eccentric centre of rotation can, therefore, be reasoned to only depend on the rotation-induced normal force $F_{N,rot}$, leading to neglect of the standard normal force F_N in the remainder of this work.

In order to investigate the fluid's local influence on the rotation-induced normal force $F_{N,rot}$, the local contributions of the torque T_y on the fragment surface are visualized in Figure 16, assuming an eccentric centre of rotation.

$|\mathbf{u}|$ in $\mathrm{m\,s^{-1}}$ $\mathbf{T_y}(x_b)$ in 10^{-11} N
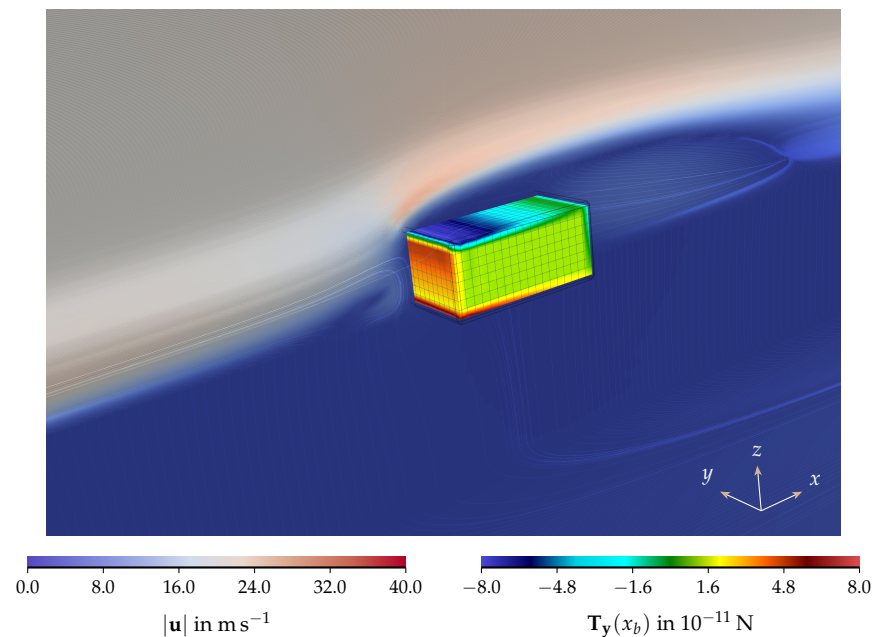
Figure 16. Detailed flow field featuring a single PM layer fragment coloured according to local contribution to torque $\mathbf{T_y}(x_b)$. Streamlines exhibit local flow direction. Left colour scale indicates local flow velocity magnitude $|\mathbf{u}|$. Porous substrate removed for visual clarity.

It can be observed that the highest force magnitude is found near the front upper edge (dark blue, dark red), which forms the starting point for the elevated fluid velocity on the fragment's upper side. The edge also represents the inflection point between positive and negative values that either contribute to the fragment's detachment or an additional support of adhesive forces that keep the fragment attached to the porous substrate. Flow conditions in this region, and all factors potentially influencing them before reaching this position, are, therefore, of specific interest for the fragment's detachment behaviour.

4.2.3. Grid Convergence

In order to access the accuracy of the hydrodynamic force, the grid convergence for the tangential and the rotation-induced normal force F_T and $F_{N,rot}$ is evaluated for different inflow velocities $\bar{u}_{in}$ and shown in Figure 17.

As predicted, it can be observed that both forces are subject to much larger fluctuations than the flow convergence quantities in the particle-free case in Figure 10 due to anisotropic discretization effects. For most velocities, however, both forces exhibit linear to quadratic convergence behaviour with a general error level below $err_{L^2} = 10^{-1}$. Considering that the presented model rather represents a real application case than a simplified benchmark case (as, e.g., considered in Trunk et al. [24] and Haussmann et al. [36]), while including both porous media modelling and the surface-resolved particle approach, this represents satisfactory accuracy. When comparing results with different inflow velocities, their apparent influence on the convergence behaviour should, nonetheless, be kept in mind. This limitation, however, is irrelevant for the following section, as an inflow velocity of $\bar{u}_{in} = 20\,\mathrm{m\,s^{-1}}$ is considered for all studies.
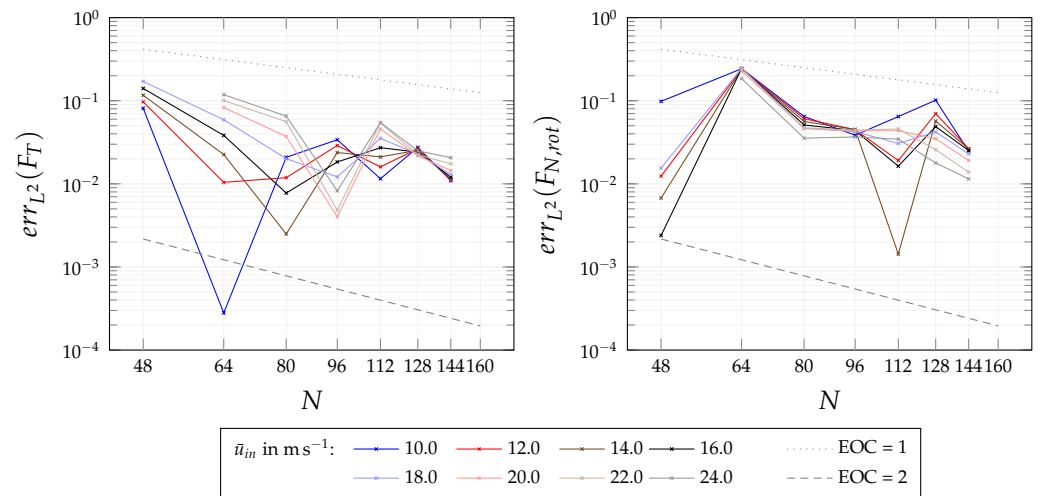
Figure 17. Error err_{L^2} of tangential and standard normal force for different inflow velocities $\bar{u}_{in}$. Reference solution χ^{ref} at $N = 160$. Quadratic and linear EOC as guidelines.

The presented quantification of stability and accuracy for both the particle-free flow in Section 3.1 and the single-layer fragment in Section 3.2 justify confidence in using the wall-flow model with elevated inflow velocities. This statement includes the specific set of boundary conditions, as well as the porous media and the resolved particle approach.

4.3. Deposition Layer during Break-Up

In this section, the results from investigating a uniformly fragmented deposition layer, as well as the impacts of the modifications described in Section 3.3, are presented. The latter comprise the influence of a uniform or increasing layer height (c.f. Sections 4.3.2 and 4.3.3), non-uniform layer fragmentation (c.f. Sections 4.3.4) and partial detachment (c.f. Sections 4.3.5). A resolution of $N = 96$ and an inflow velocity of $\bar{u}_{in} = 20\,\text{m s}^{-1}$ are selected for all studies to ensure a sufficient distance to the stability limit and feasible computation times.

4.3.1. Uniformly Fragmented Deposition Layer

A deposition layer with a significant height, covering the majority of an inlet channel's cross-section, leads to a great reduction in the volume available for the gaseous flow. The resulting flow field for such a layer is shown in Figure 18.
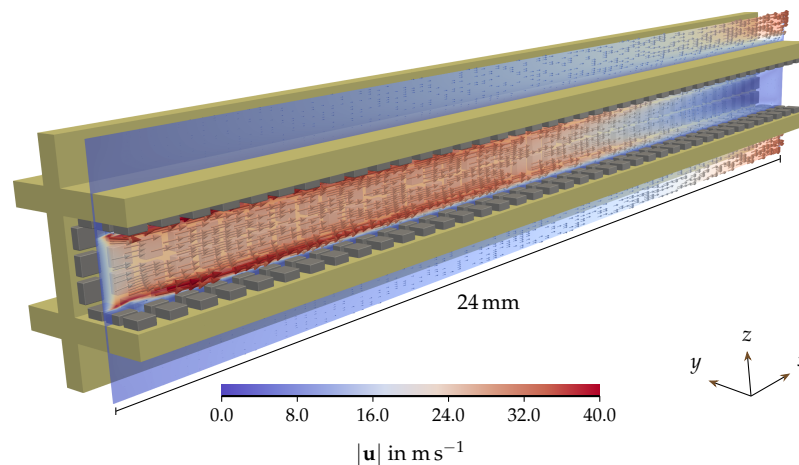
Figure 18. Flow field with uniformly fragmented PM layer in gray. Dark yellow structures represent porous filter substrate. Colour scale indicates local velocity magnitude.

Compared to the flow field in Figure 14, much higher fluid velocities of up to $|\mathbf{u}| = 40\,\text{m}\,\text{s}^{-1}$ emerge in the reduced cross-section. These form into a somewhat continuous layer of elevated fluid velocity closely above the fragmented layer over most of the channel length. Due to the cross-section's sudden reduction near the channel inlet, the flow is initially directed towards the channel's centre, leading to an arch over the first three fragment rows. A close-up, focusing on the centre fragment of the third row, is shown in Figure 19.
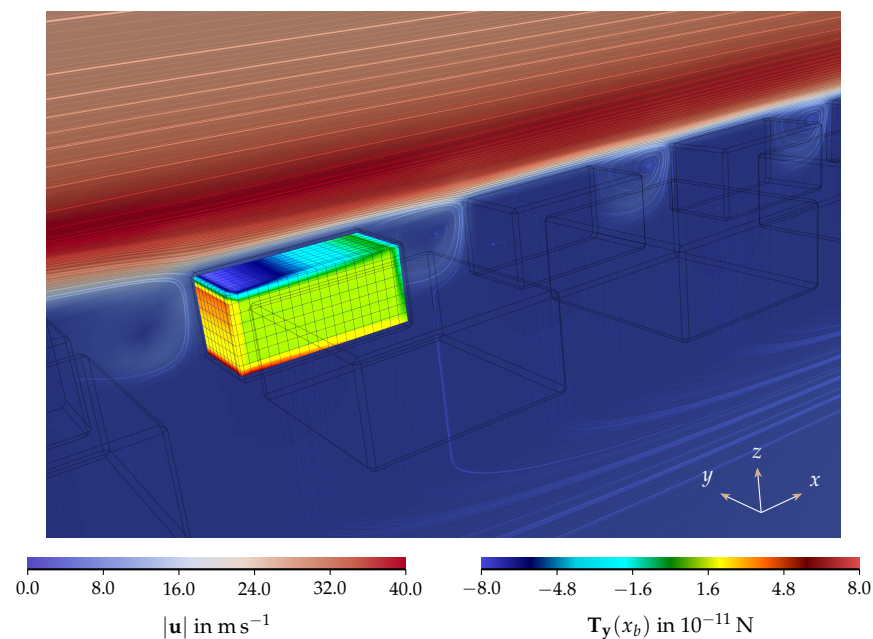
Figure 19. Detailed flow field with uniformly fragmented PM layer. Exemplary fragment coloured according to local contribution to torque $\mathbf{T_y}(x_b)$. Streamlines exhibit local flow direction. Left colour scale indicates local flow velocity magnitude $|\mathbf{u}|$. Porous substrate removed for visual clarity.

The exemplary fragment can be observed to exhibit a similar distribution of torque contributions as in the single fragment case in Figure 16. The magnitude of positive contributions on the exposed front side, however, is much smaller. The elevated velocity layer can clearly be identified on the particle's upper side, with a relatively sharp transition zone. Between the individual fragments, distinct flow structures occur, which show some resemblance to the ones obtained in a lid-driven cavity problem [37].

In order to derive predictions on the detachment likelihood of individual layer fragments, the spatial distribution of the hydrodynamic force acting on the fragments on one of the four substrate walls is retrieved. In Figure 20, the tangential force F_t and the rotation-induced normal force $F_{n,rot}$ are shown for each individual fragment along the channel length for the right, centre and left rows of the fragment field.

It becomes apparent that, contrary to the observations at smaller velocities in Hafen et al. [9], the y-position has a negligible influence, as all three rows feature a very similar profile. For both forces, the frontmost fragment row experiences much higher values, while the ones for the rotation-induced normal component exceed the tangential ones. Due to the main flow direction along the channel length, all tangential values are positive with a small decrease in the mid-channel.

However, all rotation-induced normal force values after the first fragment row stay below zero. This already implies that, independent of any normal-directed adhesion force, no detachment can occur in that region for similar configurations as long as the centre of rotation in Figure 3 does not slip. The effect of the initial arch of elevated velocities on top of the first three fragment rows, shown in Figure 18, is visible in the force values as well.
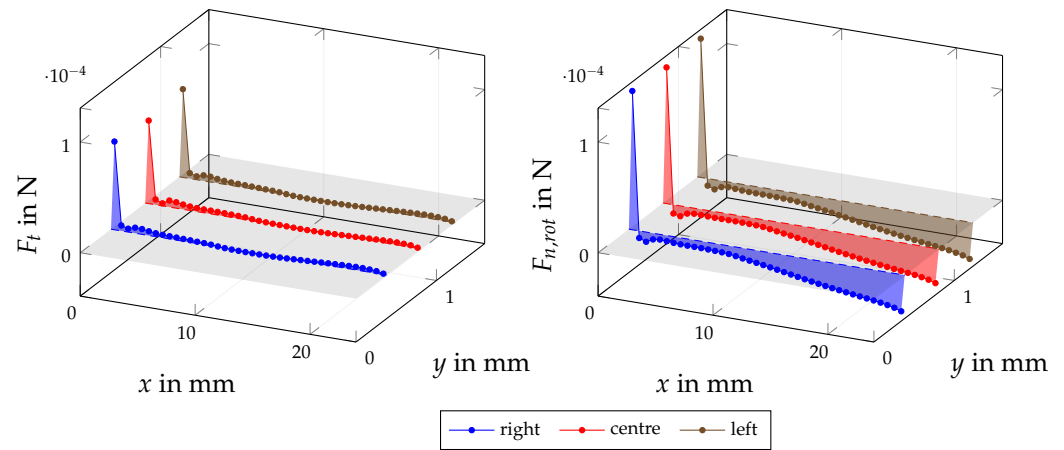
Figure 20. Two-dimensional distribution of tangential forces F_t and rotation-induced normal forces $F_{n,rot}$ in a fragmented PM layer on one of four substrate walls. Differentiation between three lateral rows. Gray plane at zero crossing.

A close-up of the different force contributions after the first row, including the standard normal force component F_N is shown in Figure 21.
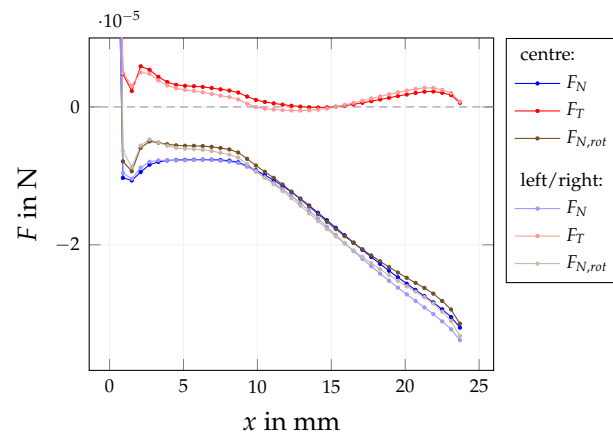
Figure 21. Distribution of tangential forces F_t, standard normal forces F_n and rotation-induced normal forces $F_{n,rot}$ in central and outer PM fragment rows.

It can be observed that the values of the centre line and the outer row indeed differ in such a small way that only the centre row is considered for all following studies. The close-up additionally reveals that the rotation-induced normal force always exceeds the standard normal force, serving as another reason to use it as the proper representative for the evaluation of *normal-directed detachment* (c.f. Section 3.2) in the following.

4.3.2. Influence of Uniform Layer Height

A change in the height of the fragmented deposition layer changes both the hydrodynamic force on the surface of a single fragment and the overall flow field due to increase in the available channel cross-section. The flow field for the smallest considered height of $d_z = 21.0 \, \mu\text{m}$ is shown in Figure 22.
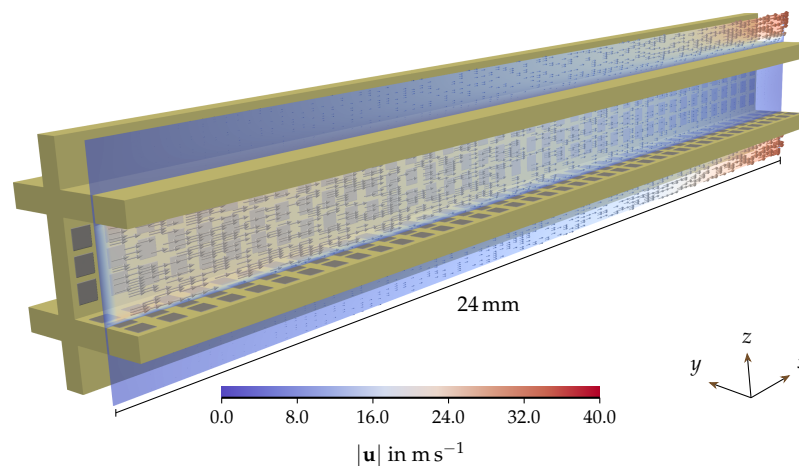
Figure 22. Flow field with fragmented PM layer assuming a height of $d_z = 21.0\,\mu m$ in gray. Dark yellow structures represent porous filter substrate. Colour scale indicates local velocity magnitude.

The thin layer results in a more homogeneous flow field with no distinct layer of elevated velocities on the fragment's upper side. A comparison of the velocity profile for different layer heights is shown in Figure 23. It should be noted at this point that all velocity contributions are still averaged over the whole channel cross-section.
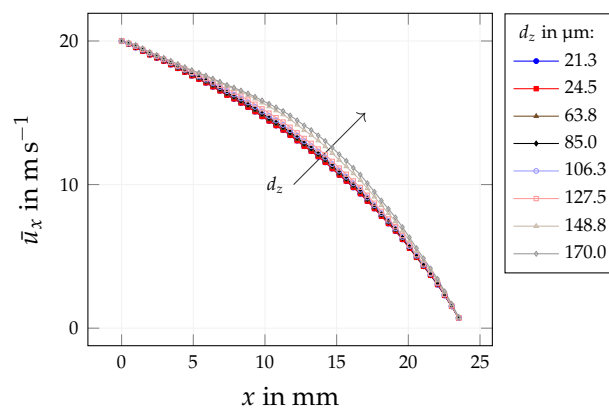
Figure 23. Velocity profiles $\bar{u}_x(x)$ in inlet channel domain.

It can be observed that the development of the averaged fluid velocity in the main flow direction is not influenced significantly, despite potentially large differences in local velocity contributions. The resulting hydrodynamic forces for different layer heights are shown in Figure 24.

The greatest impact of the fragment height can be found in the first row due to the great flow exposition, while the following fragments are less affected. These exhibit only negative contributions for the rotation-induced normal force, independent of the considered layer height. For the thinnest layer, this is additionally true for the first row, rendering normal-directed detachment unlikely.
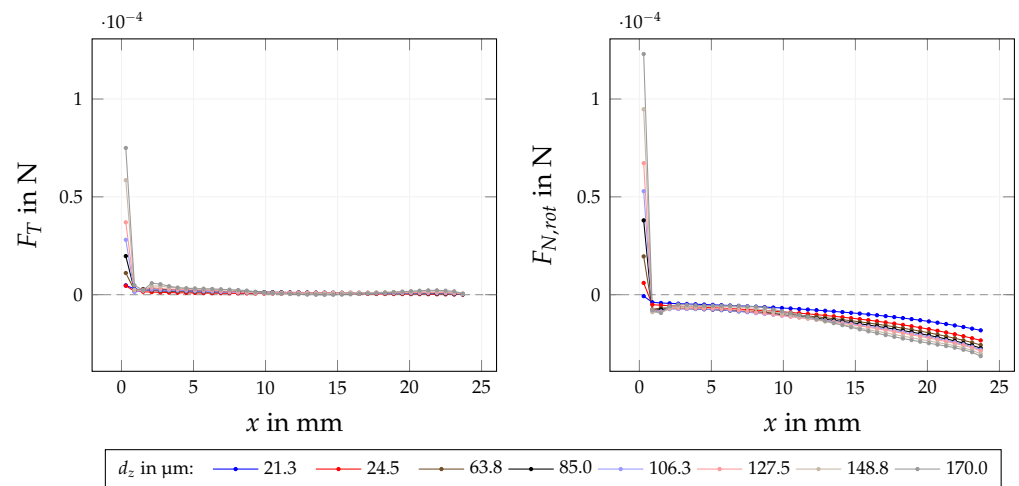
Figure 24. Distribution of tangential forces F_t and rotation-induced normal forces $F_{n,rot}$ in central PM fragment row for different uniform layer heights d_z.

4.3.3. Influence of Increasing Layer Height

A less prominent flow exposition of the first particle row results from a less abrupt decrease in the channel's cross-section due to a gradually increasing layer height. The flow field for a smooth transition from $d_z = 0.0425$ mm to 0.17 mm over a relative channel length of $x_{rel} = 0.4$ is shown in Figure 25.
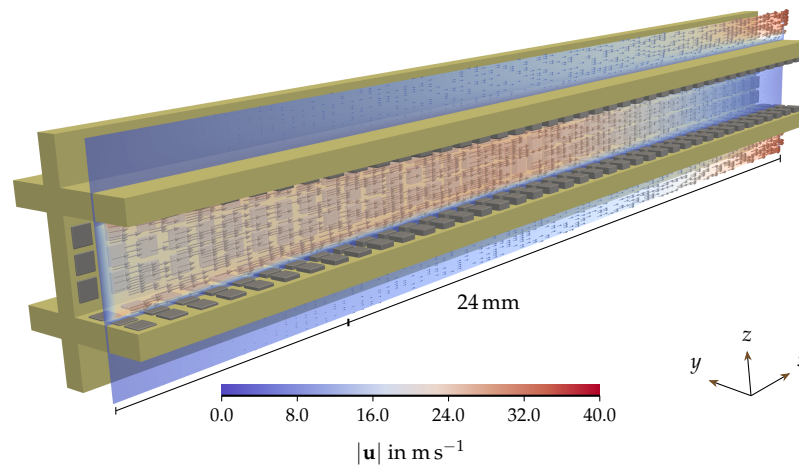
Figure 25. Flow field with fragmented PM layer assuming an increasing height over a relative channel length of $x_{rel} = 0.4$ in gray. Dark yellow structures represent porous filter substrate. Colour scale indicates local velocity magnitude.

The channel's front appears similar to the uniform thin layer in Figure 22; however, an increase in the velocity magnitude can be observed in the mid-channel.

As the fluid slows down again towards the channel's back, entrained PM fragments are expected to experience the strongest acceleration in the channel's mid-section once detached. The force distribution is shown in Figure 26.
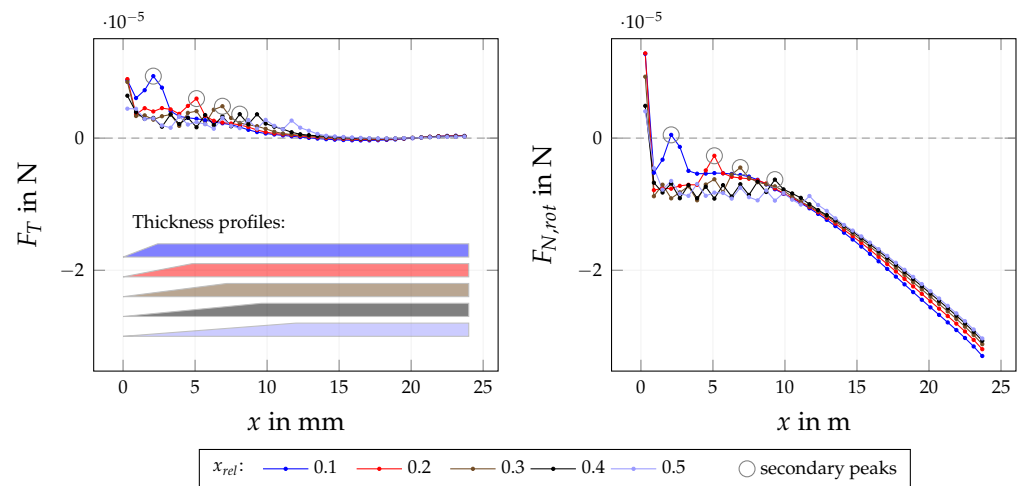
Figure 26. Distribution of tangential forces F_t and rotation-induced normal forces $F_{n,rot}$ in central PM fragment row with increasing height over different relative channel lengths x_{rel}. Sketches (left) lay out height profiles. Circular marks indicate secondary peaks.

The distribution of both forces is more homogeneous with respect to the previously investigated layers. While the rotation-induced normal force $F_{N,rot}$ still features the distinct force signal in the first row, the tangential force F_T shows a rather gradual decrease. When considering a sufficiently steep increase in height ($x_{rel} \leq 0.4$), a secondary peak emerges in both force signals at the transition point to a uniform layer height. None of the peaks, however, features significant positive values for the rotation-induced normal force to favour detachment.

4.3.4. Influence of Non-Uniform Layer Fragmentation

All the previously investigated layer variants represent the same coverage of the porous filter substrate. In order to investigate the coverage influence on both the fluid field and the hydrodynamic forces, linearly increasing or decreasing fragment sizes are considered while assuming the same height. Figure 27 shows the flow field for an increasing coverage, starting with a relative fragment size of $d_{xy,rel} = 0.6$ with respect to the standard dimension of $340 \times 340 \times 170\,\mu m^3$ (c.f. Section 3.2).
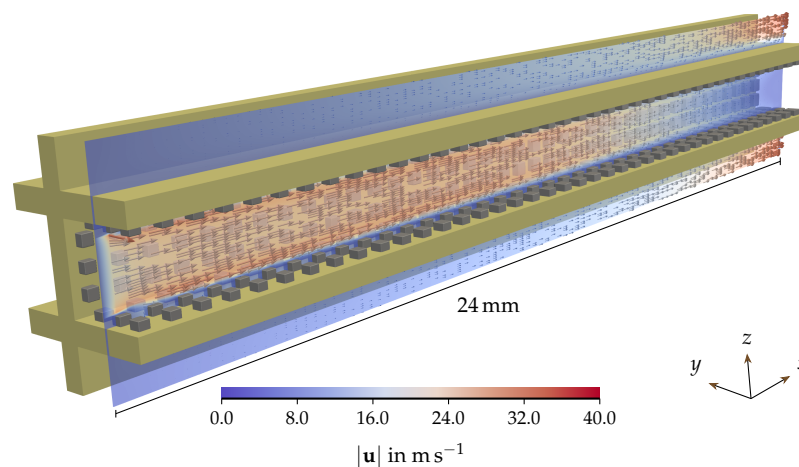
Figure 27. Flow field with fragmented PM layer assuming an increasing substrate coverage beginning from a relative fragment size of $d_{xy,rel} = 0.6$ in gray. Dark yellow structures represent porous filter substrate. Colour scale indicates local velocity magnitude.

It can be observed that the increased cross-section in the channel's front prevents the formation of an elevated velocity layer, as found in Figure 18. The distribution of the

velocity magnitude, therefore, appears very homogeneous over the first two-thirds of the channel length, leading to a nearly constant acceleration regime detached particles would be exposed to.

In order to quantify the coverage influence for each relative fragment size $d_{xy,rel}$, the decreasing case is related to the increasing one by subtracting the velocity profiles of the latter from the prior. The velocity differences are shown in Figure 28.
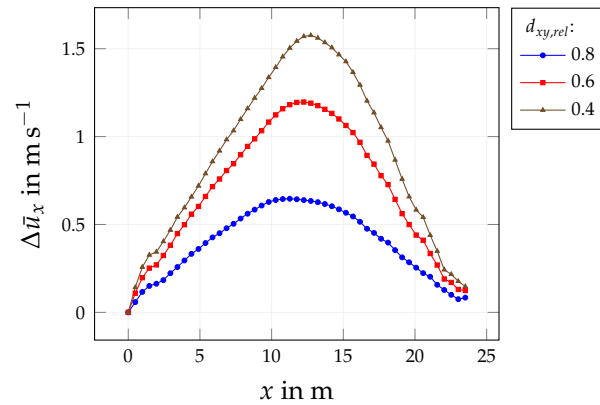
Figure 28. Difference between velocity profiles $\bar{u}_x(x)$ of increasing and decreasing coverage for different relative fragment sizes $d_{xy,rel}$ in inlet channel domain.

It can be seen that the subtraction of the profiles yields only positive values. This means that a smaller fragment size in the front section (in the increasing case) leads to a smaller average fluid velocity over most of the channel length. The maximum of the velocity difference $\Delta \bar{u}_x$ can be found in the mid-section of the channel. This represents a wall-flow-specific feature, as the coverage between increasing and decreasing configuration for the same relative fragment size $d_{xy,rel}$ differs most at the channel's front and its back, but is in fact identical in mid-channel. This implies that more of the flow passes through the substrate's front section when the coverage is smaller in this area. With larger differences in the particle dimensions, the peak increases and slightly moves towards the back of the channel. In any case, the values of the velocity difference $\Delta \bar{u}_x$ can be considered relatively small with respect to the inflow velocity of $\bar{u}_{in} = 20\,\mathrm{m\,s^{-1}}$.

The respective force distributions are shown in Figure 29.
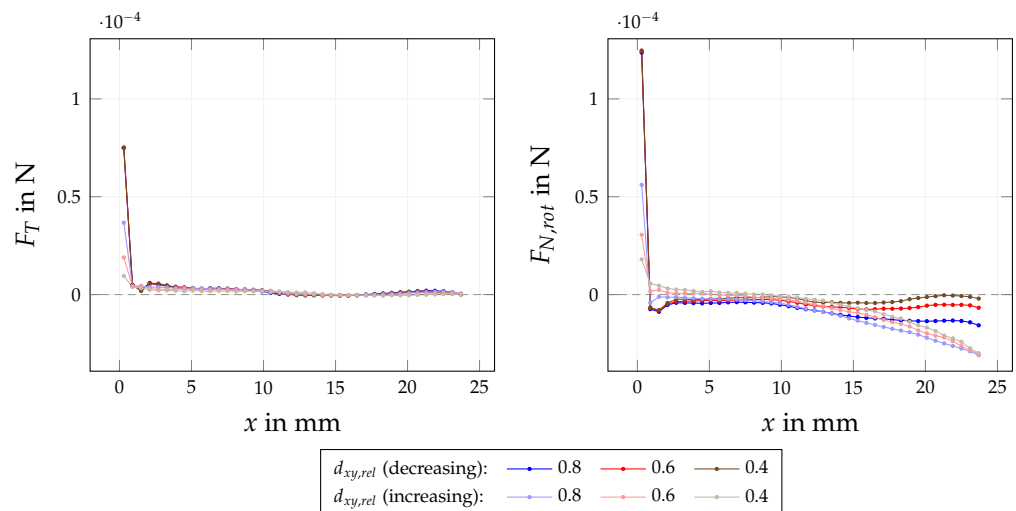
Figure 29. Distribution of tangential forces F_t and rotation-induced normal forces $F_{n,rot}$ in central PM fragment row with increasing and decreasing substrate coverage beginning from or ending with different relative fragment sizes $d_{xy,rel}$.

The values of the first row are not affected by the decreasing coverage, which mainly leads to differences in the channel back. In the increasing case, in turn, the values of the first row directly depend on the fragment size and exhibit smaller force signals accordingly when considering smaller relative fragment sizes $d_{xy,rel}$. It is, however, noteworthy that, for sufficiently small fragment sizes below $d_{xy,rel} = 0.6$, a significant amount of slightly positive values of the rotation-induced normal force can be found even after the first row. Provided there are very small adhesive forces, this potentially enables the simultaneous detachment of multiple fragments in this region.

4.3.5. Influence of Partial Detachment

Due to the prominent role of the first fragment row in all previous studies, the effect of a fragmented layer with significant partial detachment in the front section is investigated. The flow field assuming a partial detachment up to a relative channel length of $x_{rel} = 0.1$ is shown in Figure 30.
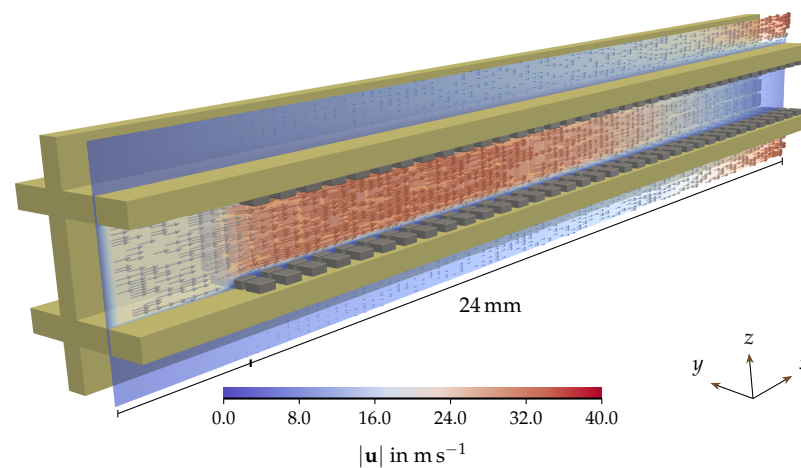
Figure 30. Flow field with fragmented PM layer assuming partial detachment over a relative channel length of $x_{rel} = 0.1$ in gray. Dark yellow structures represent porous filter substrate. Colour scale indicates local velocity magnitude.

The transition point between the particle free substrate area to the first fragment row is characterized by a great increase in the fluid velocity magnitude due to the abrupt change in the cross-section available for the gaseous flow. Unlike the full uniformly fragmented deposition layer in Figure 18, however, a layer of elevated velocity does not appear and the fluid velocity features a homogeneous cross-section over the whole inflow channel. Considering the fact that the layer of elevated fluid velocity in the full layer case was observed over most of the channel length, it can be reasoned that a partial detachment of the first fragment rows leads to a homogenization of the whole fluid field. The force distributions assuming partial detachment up to various relative channel lengths x_{rel} are shown in Figure 31.

It can be observed that the appearance of relatively high force values at the first row do not depend on its overall position in the existing flow field, but can be attributed to its exposed position in the flow. First rows located further towards the channel end do, however, experience smaller forces. The trend continues until negative values result for the rotation-induced normal force $F_{n,rot}$ after a relative channel length of $x_{rel} = 0.5$. This implies that PM fragments in a uniformly fragmented layer most likely detach one row after another until a threshold position is reached beyond which detachment can not occur any more.
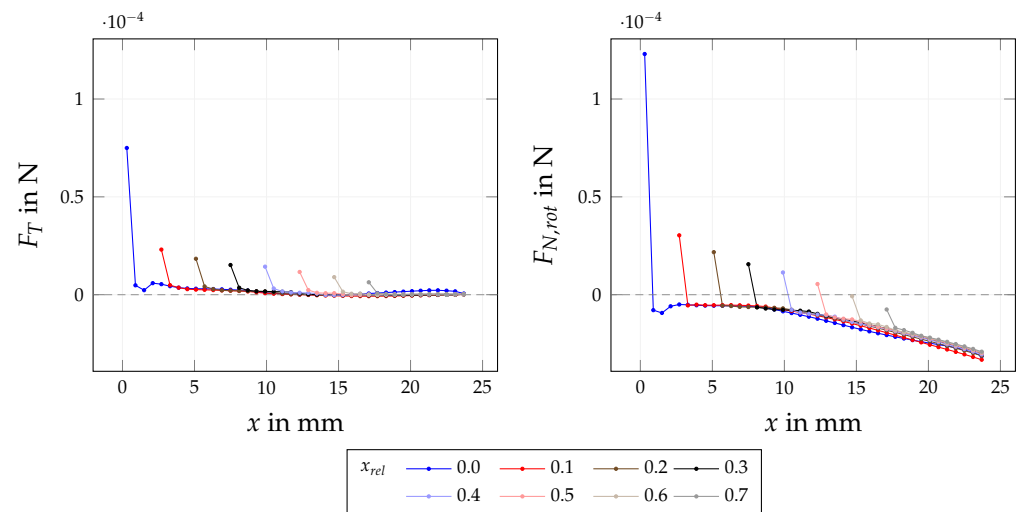
Figure 31. Distribution of tangential forces F_t and rotation-induced normal forces $F_{n,rot}$ in central PM fragment row with partial detachment over different relative channel lengths x_{rel}.

5. Conclusions

The present work investigates the PM structure detachment from surfaces of wall-flow filters for elevated velocities using a previously developed LBM approach. Three different scenarios were investigated: The *particle-free flow* in a clean channel was examined with respect to the parameter domain that ensures sufficient stability and accuracy. By evaluating the simulations' final states, a necessary stability domain was defined and a resolution-dependent expression for a stability threshold for the average inflow velocity was obtained. For grid resolutions of at least $N = 96$ cells per channel diameter, reasonable velocity and pressure accuracy could be achieved, including a satisfactory mass conservation. The parameter domain was then reevaluated for the flow around a *single layer fragment*, attached to the porous wall's substrate, including the individual components of the hydrodynamic surface force. It could be shown that the suitable parameter domain was limited to inflow velocities below $\bar{u}_{in} = 28\,\text{m}\,\text{s}^{-1}$. The flow field was shown to feature distinct regions of increased and decreased local fluid velocities in the fragment's vicinity. Furthermore, the rotation-induced normal force was reasoned to be the relevant one for the prediction of fragment detachment. The force contributions could be shown to feature satisfactory accuracy for the wall-flow model with porous media and the surface-resolved particle approach included. With the wall-flow model's stability and accuracy for elevated velocities ensured, a *deposition layer during break-up* was investigated regarding local effects on the fluid field and the acting forces for different situations. Predictions on the detachment likelihood of individual layer fragments and their mutual influence were derived based on the spatial distribution of hydrodynamic forces. A uniformly fragmented PM layer of considerable height could be shown to lead to local velocity magnitudes of up to twice as large as the average inflow velocity. The first fragment row was identified as especially prone to detachment, with the following fragments being rather shielded. Contrary to previous observations [9], in low-velocity regimes, no significant dependency on the *y*-position along the channel width was noticeable. The layer height could be shown to predominantly have an effect on the first fragment row, while the impact could be observed to be diminished when considering continuously increasing layer heights. The substrate coverage turned out to have a minor effect on the velocity profile along the channel length, but was shown to potentially enable simultaneous detachment over multiple fragment rows when considering a sufficiently small coverage in the channel's front. Eventually, it could be shown that all considered cases do not significantly change the fact that normal directed detachment most likely occurs row-for-row until non-detachable rows are reached in the channel back.

The presented work provides a detailed quantification of stability and accuracy for static, impermeable PM layer fragments attached to the porous substrate's surface inside a single channel of a wall-flow filter. Furthermore, it provides relevant insights into the nature of the hydrodynamic forces acting on the particulate structures and the local detachment likelihood of individual layer fragments depending on local flow conditions and the layer's fragmentation. As these represent key factors for rearrangement events and respective deposition pattern predictions, they contribute to potential optimizations in engine performance, fuel consumption and the service life of wall-flow filters.

Author Contributions: Conceptualization, N.H., A.D. and M.J.K.; methodology, N.H., J.E.M., A.D. and M.J.K.; software, N.H., J.E.M. and M.J.K.; validation, N.H.; formal analysis, N.H., J.E.M., A.D. and M.J.K.; investigation, N.H.; resources, A.D. and M.J.K.; data curation, N.H.; writing—original draft preparation, N.H.; writing—review and editing, N.H., J.E.M., A.D. and M.J.K.; visualization, N.H.; supervision, A.D. and M.J.K.; project administration, N.H., A.D. and M.J.K.; funding acquisition, N.H., A.D. and M.J.K. All authors have read and agreed to the published version of the manuscript.

Funding: This research was funded by the Deutsche Forschungsgemeinschaft (DFG, German Research Foundation)—422374351.

Data Availability Statement: Not applicable.

Acknowledgments: We acknowledge support by the KIT-Publication Fund of the Karlsruhe Institute of Technology. This work was performed on the HoreKa supercomputer funded by the Ministry of Science, Research and the Arts Baden-Württemberg and by the Federal Ministry of Education and Research.

Conflicts of Interest: The authors declare no conflict of interest.

Abbreviations

The following abbreviations are used in this manuscript:

BGK	Bhatnagar–Gross–Krook
EOC	experimental order of convergence
FVM	finite volume method
HLBM	homogenized lattice Boltzmann method
LBE	lattice Boltzmann equation
LBM	lattice Boltzmann method
NSE	Navier–Stokes equation
PM	particulate matter
PSM	partially saturated method

Nomenclature

The following symbols are used in this manuscript:

$\boldsymbol{u}$	fluid velocity	$\Delta l_{w,max}$	distance to wall at peak velocity
p	fluid pressure	$\Delta l_{w,0}$	distance to wall at starting position
ρ	fluid density	Δl_s	stopping distance
ν	kinematic fluid viscosity	F_D	drag force
$\boldsymbol{x}$	position	d_p	diameter of reference sphere
t	time	χ	generic flow quantity
δx	discrete spacing of voxel mesh	$\bar{\chi}$	average of generic flow quantity
δt	discrete time step	σ	standard deviation of flow quantity
N	resolution of voxel mesh	r	residuum of flow quantity
D	number of spacial dimensions	T	number of last time steps
q	number of discrete velocities	M	total cell number
$\boldsymbol{c}_i$	discrete velocity	l_x	channel length
f	distribution function	l_y	channel width

f_i	discrete-velocity distribution function	l_z	channel height
$f_i^{(eq)}$	discrete-velocity equilibrium distribution function	s_l	length scaling factor
Ω_i	discrete collision operator	$l_{x,s}$	scaled channel length
τ	lattice relaxation time	$\bar{u}_{in}$	average inflow velocity
w_i	weight of discrete lattice velocity	$\bar{u}_w$	average wall penetrating velocity
c_s	lattice speed of sound	$x_{p,0}$	particle starting position (before detachment)
K	permeability	$\boldsymbol{F}_0$	initial force (before detachment)
K_{min}	minimum permeability	ρ_p	particle density
d	confined permeability	NOC	number of cells
$\boldsymbol{u}^{eff}$	effective velocity	d_x	fragment's x-dimension
B	local weighting factor	d_y	fragment's y-dimension
$\boldsymbol{u}^S$	velocity at solid particle node	d_z	fragment's z-dimension
k	particle index	$d_{xy,rel}$	fragment's x- and y-dimension
X_k	particle's centre of mass	$F_{N,rot}$	rotation-induced normal force
$\vec{x}$	point on outward-facing normal of surface	x_{rel}	relative position along channel length
ϵ	width of smooth transition layer	n_p	number of particles
$\boldsymbol{x}_b$	position of discrete particle boundary node	$n_{p,y}$	number of particles over channel width
$\boldsymbol{F}_k$	force acting on particle's centre of mass	$n_{p,x}$	number of particles over channel length
$\boldsymbol{T}_k$	torque acting on particle's centre of mass	t_{max}	maximum simulation time
m_p	particle mass	C_{in}	inlet channel domain
$u_{p,init}$	initial particle velocity	C_{out}	outlet channel domain
u_{rel}	relative particle velocity w. r. t. fluid		

References

1. Wang, Y.; Kamp, C.J.; Wang, Y.; Toops, T.J.; Su, C.; Wang, R.; Gong, J.; Wong, V.W. The origin, transport, and evolution of ash in engine particulate filters. *Appl. Energy* **2020**, *263*, 114631. [CrossRef]
2. Gaiser, G. Berechnung von Druckverlust, Ruß- und Ascheverteilung in Partikelfiltern. *MTZ Mot. Z.* **2005**, *66*, 92–102. [CrossRef]
3. Sappok, A.; Govani, I.; Kamp, C.; Wang, Y.; Wong, V. In-Situ Optical Analysis of Ash Formation and Transport in Diesel Particulate Filters During Active and Passive DPF Regeneration Processes. *SAE Int. J. Fuels Lubr.* **2013**, *6*, 336–349. [CrossRef]
4. Ishizawa, T.; Yamane, H.; Satoh, H.; Sekiguchi, K.; Arai, M.; Yoshimoto, N.; Inoue, T. Investigation into Ash Loading and Its Relationship to DPF Regeneration Method. *SAE Int. J. Commer. Veh.* **2009**, *2*, 164–175. [CrossRef]
5. Aravelli, K.; Heibel, A. Improved Lifetime Pressure Drop Management for Robust Cordierite (RC) Filters with Asymmetric Cell Technology (ACT). In Proceedings of the SAE World Congress & Exhibition, Nottingham, UK, 20–24 May 2007; SAE International: Warrendale, PA, USA, 2007. [CrossRef]
6. Dittler, A. Ash Transport in Diesel Particle Filters. In Proceedings of the SAE 2012 International Powertrains, Fuels & Lubricants Meeting, Malmo, Sweden, 18–20 September 2012; SAE International: Warrendale, PA, USA, 2012. [CrossRef]
7. Dittler, A. *Abgasnachbehandlung mit Partikelfiltersystemen in Nutzfahrzeugen*, 1st ed.; Wuppertaler Reihe zur Umweltsicherheit, Shaker: Herzogenrath, Germany, 2014.
8. Wang, Y.; Kamp, C. The Effects of Mid-Channel Ash Plug on DPF Pressure Drop. In Proceedings of the SAE 2016 World Congress and Exhibition, Detroit, MI, USA, 12–14 April 2016; SAE International: Warrendale, PA, USA, 2016. [CrossRef]
9. Hafen, N.; Dittler, A.; Krause, M.J. Simulation of particulate matter structure detachment from surfaces of wall-flow filters applying lattice Boltzmann methods. *Comput. Fluids* **2022**, *239*, 105381. [CrossRef]
10. Konstandopoulos, A.G.; Skaperdas, E.; Warren, J.; Allansson, R. Optimized Filter Design and Selection Criteria for Continuously Regenerating Diesel Particulate Traps. In Proceedings of the International Congress & Exposition, Fort Lauderdale, FL, USA, 6–8 December 1999; SAE International: Warrendale, PA, USA, 1999. [CrossRef]
11. Hafen, N.; Thieringer, J.R.; Meyer, J.; Krause, M.J.; Dittler, A. Numerical investigation of detachment and transport of particulate structures in wall-flow filters using lattice Boltzmann methods. *J. Fluid Mech.* **2023**, *956*, A30. [CrossRef]
12. Thieringer, J.R.D.; Hafen, N.; Meyer, J.; Krause, M.J.; Dittler, A. Investigation of the Rearrangement of Reactive ash; Inert Particulate Structures in a Single Channel of a Wall-Flow Filter. *Separations* **2022**, *9*, 195. [CrossRef]
13. Krüger, T.; Kusumaatmaja, H.; Kuzmin, A.; Shardt, O.; Silva, G.; Viggen, E.M. *The Lattice Boltzmann Method—Principles and Practice*; Springer: Cham, Switzerland, 2016. [CrossRef]
14. Ferziger, J.H.; Perić, M. *Numerische Strömungsmechanik*; Springer: Berlin/Heidelberg, Germany, 2008. [CrossRef]
15. Brinkman, H.C. A calculation of the viscous force exerted by a flowing fluid on a dense swarm of particles. *Flow Turbul. Combust.* **1949**, *1*, 27. [CrossRef]
16. Bhatnagar, P.L.; Gross, E.P.; Krook, M. A Model for Collision Processes in Gases. I. Small Amplitude Processes in Charged and Neutral One-Component Systems. *Phys. Rev.* **1954**, *94*, 511–525. [CrossRef]

17. Ginzburg, I. Equilibrium-type and link-type lattice Boltzmann models for generic advection and anisotropic-dispersion equation. *Adv. Water Resour.* **2005**, *28*, 1171–1195. [CrossRef]

18. Simonis, S.; Haussmann, M.; Kronberg, L.; Dörfler, W.; Krause, M. Linear and brute force stability of orthogonal moment multiple–relaxation–time lattice Boltzmann methods applied to homogeneous isotropic turbulence. *Philos. Trans. R. Soc. Math. Phys. Eng. Sci.* **2021**, *379*, 20200405.

19. Hafen, N.; Krause, M.J.; Dittler, A. Simulation of Particle-Agglomerate Transport in a Particle Filter using Lattice Boltzmann Methods. In Proceedings of the 22th Internationales Stuttgarter Symposium, Stuttgart, Germany, 15–16 March 2022; Bargende, M., Reuss, H.C., Wagner, A., Eds.; Springer: Wiesbaden, Germany, 2022; pp. 292–303.

20. Chapman, S.; Cowling, T.; Burnett, D.; Cercignani, C. *The Mathematical Theory of Non-uniform Gases: An Account of the Kinetic Theory of Viscosity, Thermal Conduction and Diffusion in Gases*; Cambridge Mathematical Library, Cambridge University Press: Cambridge, UK, 1990.

21. Krause, M.J.; Kummerländer, A.; Avis, S.J.; Kusumaatmaja, H.; Dapelo, D.; Klemens, F.; Gaedtke, M.; Hafen, N.; Mink, A.; Trunk, R.; et al. OpenLB—Open source lattice Boltzmann code. Development and Application of Open-source Software for Problems with Numerical PDEs. *Comput. Math. Appl.* **2021**, *81*, 258–288. [CrossRef]

22. Spaid, M.A.A.; Phelan, F.R. Lattice Boltzmann methods for modeling microscale flow in fibrous porous media. *Phys. Fluids* **1997**, *9*, 2468–2474.

23. Krause, M.J.; Klemens, F.; Henn, T.; Trunk, R.; Nirschl, H. Particle flow simulations with homogenised lattice Boltzmann methods. *Particuology* **2017**, *34*, 1–13. [CrossRef]

24. Trunk, R.; Marquardt, J.; Thäter, G.; Nirschl, H.; Krause, M.J. Towards the simulation of arbitrarily shaped 3D particles using a homogenised lattice Boltzmann method. *Comput. Fluids* **2018**, *172*, 621–631. [CrossRef]

25. Trunk, R.; Weckerle, T.; Hafen, N.; Thäter, G.; Nirschl, H.; Krause, M.J. Revisiting the Homogenized Lattice Boltzmann Method with Applications on Particulate Flows. *Computation* **2021**, *9*, 11. [CrossRef]

26. Noble, D.R.; Torczynski, J.R. A Lattice-Boltzmann Method for Partially Saturated Computational Cells. *Int. J. Mod. Phys. C* **1998**, *9*, 1189–1201.

27. Rettinger, C.; Rüde, U. A comparative study of fluid-particle coupling methods for fully resolved lattice Boltzmann simulations. *Comput. Fluids* **2017**, *154*, 74–89. [CrossRef]

28. Liu, J.; Huang, C.; Chai, Z.; Shi, B. A diffuse-interface lattice Boltzmann method for fluid–particle interaction problems. *Comput. Fluids* **2022**, *233*, 105240. [CrossRef]

29. Marquardt, J.E.; Römer, U.J.; Nirschl, H.; Krause, M.J. A discrete contact model for complex arbitrary-shaped convex geometries. *Particuology* **2023**, *80*, 180–191. [CrossRef]

30. Wen, B.; Zhang, C.; Tu, Y.; Wang, C.; Fang, H. Galilean invariant fluid–solid interfacial dynamics in lattice Boltzmann simulations. *J. Comput. Phys.* **2014**, *266*, 161–170. [CrossRef]

31. Ladd, A.J.C. Numerical simulations of particulate suspensions via a discretized Boltzmann equation. Part 1. Theoretical foundation. *J. Fluid Mech.* **1994**, *271*, 285–309. [CrossRef]

32. Latt, J.; Chopard, B.; Malaspinas, O.; Deville, M.; Michler, A. Straight velocity boundaries in the lattice Boltzmann method. *Phys. Rev. E* **2008**, *77*, 056703. [CrossRef] [PubMed]

33. Skordos, P.A. Initial and boundary conditions for the lattice Boltzmann method. *Phys. Rev. E* **1993**, *48*, 4823–4842. [CrossRef]

34. Sappok, A.; Kamp, C.; Wong, V. Sensitivity Analysis of Ash Packing and Distribution in Diesel Particulate Filters to Transient Changes in Exhaust Conditions. *SAE Int. J. Fuels Lubr.* **2012**, *5*, 733–750. [CrossRef]

35. Zhao, C.; Zhu, Y.; Huang, S. Pressure Drop and Soot Accumulation Characteristics through Diesel Particulate Filters Considering Various Soot and Ash Distribution Types. In Proceedings of the WCX™ 17: SAE World Congress Experience, Detroit, MI, USA, 4–6 April 2017; SAE International: Warrendale, PA, USA, 2017. [CrossRef]

36. Haussmann, M.; Hafen, N.; Raichle, F.; Trunk, R.; Nirschl, H.; Krause, M.J. Galilean invariance study on different lattice Boltzmann fluid–solid interface approaches for vortex-induced vibrations. *Comput. Math. Appl.* **2020**, *80*, 671–691. [CrossRef]

37. Ghia, U.; Ghia, K.; Shin, C. High-Re solutions for incompressible flow using the Navier-Stokes equations and a multigrid method. *J. Comput. Phys.* **1982**, *48*, 387–411. [CrossRef]